A Numerical Study on Suspended Sediment Transport in a Partially Vegetated Channel Flow

Mingyang Wang[1], Eldad Avital*[1], Qingsheng Chen[2], John Williams[1], Shuo Mi[1], Qiancheng Xie[3]

1. School of Engineering and Materials Science, Queen Mary, University of London, UK
2. College of Water Conservancy and Hydropower Engineering, Hohai University, China
3. Division of Fluid and Experimental Mechanics, Luleå University of Technology, Sweden
*. Author to whom correspondence should be addressed

Abstract

Turbulent structures generated by vegetation patches play a dominant role in the dispersion of suspended sediment, which in turn is of great significance for ecosystem cycling and river geomorphology development. High fidelity Large Eddy Simulations (LES) coupled with the Discrete Phase Method (DPM) were used to explore the particle distribution and its variance (the non-uniformity in temporal and spatial space) in a partially vegetated straight channel. The novel findings and conclusions are outlined here. Firstly, the contour of the vertical vorticity component coincides well with particle preferential gatherings in the outer edge of the mixing layer in the near-bed region. Large-scale turbulent structures grow in mixing layer along the side of a vegetation patch (VP), which deplete particles away from the mixing layer into the neighbouring region. Also, higher vegetation densities (*Dn*) promote this depletion trend. Secondly, the Probability Density Function (PDF) and its variance were defined to quantify these phenomena, illustrating that the VP continuously interrupts the flow condition and promotes higher non-uniformity of particle distribution among the vegetated and non-vegetated regions. The variance of the PDF in the non-vegetated region is significantly higher than that in the neighbouring vegetated region located in the same streamwise location. The particle parcels are highly unevenly located along the periphery of the large eddies and are exchanged by the mixing flow between the non-vegetated and vegetated regions. Finally, the vertical entrainment of particles occurs in the vegetated region of the present cases. This is because the horseshoe structures provide an upwards velocity for the current *Dn* conditions ($Dn<0.1$) and an increase of *Dn* ($Dn<0.1$) accelerates the upward suspension. These findings complete our understanding of particles' transportation in both spanwise and vertical

directions.

Keywords

Suspended sediment transport; Partially vegetated channel; Turbulent structures; Probability Density Function (PDF); Variance of PDF; Particle vertical entrainment.

1. Introduction

Aquatic vegetation plays critical functions in an ecosystem of river networks and coastal regions by absorbing organic matter, producing oxygen, and supporting habitat diversity (Follett and Nepf, 2012, Rominger et al., 2010, Kemp et al., 2000). The flow resistance of vegetation dramatically decreases the flow velocity, resulting in a reduction in bed shear stresses (Stephan and Gutknecht, 2002). Vegetation patches (VPs) or riparian vegetation strongly alter turbulent structures, which is indicated by water flumes experiments partially covered by artificial vegetation (Chen et al., 2011) or by observations in natural rivers occupied by real-scale vegetation (Zhang et al., 2020, Cameron et al., 2013, Leonard et al., 2006). The turbulent structures generated by real aquatic plants are far more complex than that of artificial cylinder array (Zhang et al., 2020). In the vegetated region, a lower spatial-averaged velocity field occurs, compared to the non-vegetated channel region although it usually experiences a higher turbulent kinetic energy which may transfer bedload to suspended load (Tseng et al., 2021, Zhang et al., 2020, Yang, et al., 2016, Ortiz et al., 2013). Some researchers (Luhar et al, 2008, Van Katwijk et al., 2010, Lawson et al., 2012) observed the resuspension effects of VPs in natural waterways apart from the deposition effects of VPs, as found by other researchers (Ward et al,1984, Garcia et al., 1999, Terrados and Duarte 2000, Gacia and Duarte, 2001, Agawin and Duarte, 2002). Nonetheless, vegetation regions contain more particles and nutrient contents because of retention effects (Clarke and Wharton, 2001, Larsen et al., 2009).

During a long period of sediment retention and deposition, the morphology of a riverbed eventually changes. The presence of vegetation can stabilize a channel bed in the vegetated region and promote the growth of landform (Corenblit et al. 2007). Nevertheless, an erosion event can also occur in the leading and side edges of VP (Kim et al, 2015, Follett and Nepf, 2012). This is because the diverging flow bypasses the leading edge and speeds up in the nearby non-vegetated channel (Huai et al., 2015). Many researchers (Curran and Hession, 2013, Mars et al., 1999, Pollen and Simon, 2005) argued that river restoration and management could take advantage of the ecological and physical functions of aquatic vegetation, and research on vegetation flow was meaningful and urgent. For example, better insights of the flow and particle dynamics mechanism can help to implement a new national development strategy for the biggest sandy river in the north of China, i.e., the Yellow River Basin Ecological Protection and High-quality Development (China, 2019). However, the understanding of the interactions between the flow, vegetation and sediment transport is still limited, especially for partially vegetated channel flow with heterogeneous riverbed roughness which is ubiquitous in nature. Previous studies on vegetated sandy flow mainly focused on the vertical concentration profile of suspended load above a uniform canopy (Li et al., 2020, Huai et al., 2020, Huai et al., 2019, Lu, 2008, López and García, 1998), and were quite limited on the investigation of the horizontal distribution of the suspended load in a partial vegetated channel flow.

Constructive results for the long-term sedimentation effect on the morphodynamics in a partially vegetated river have been achieved for both off-bank and bankside VPs. The off-bank VP located in a central channel was usually simplified into a porous cylinder (Zong and Nepf, 2012). The effects of bleeding flow and wakes behind the VP on sediment transport were the focuses of previous studies (Kim et al., 2015, Ortiz et al., 2013, Zong and Nepf, 2012, Rominger et al., 2010). The bleeding flow was generated by the streamwise incoming flow penetrating through the vegetation patch. These bleeding flows always lead to a delay in the onset of vortex shedding. As the vegetation density (*Dn*) increased, the beginning point of the vortex shedding point approached the patch, but the deposition location of particles moved downstream (Follett and Nepf, 2012).

Previous investigations focused on the bankside VP located along a channel bank. The hydrodynamics and turbulent structures have been carefully studied (Huai et al., 2015, Nepf, 2012, White and Nepf, H. 2008, White and Nepf, 2007) to enhance the understanding of sediment transportation in the VP. Two main features of the flow were identified. (1) The diverging flow at the leading edge. (2) The mixing layer development as affected by Kelvin-Helmholtz instability (Zong and Nepf, 2010). Due to these features, the spatial distribution of net deposition in the VP is dominated by the streamwise flow advection and the spanwise flow dispersion governed by diverging flows and mixing layer vortices, respectively. However, in both types of VP locations (bankside and off-bank), previous studies (Gu et al., 2019, Liu and Nepf, 2016, Bertoldi et al, 2015, Follett and Nepf, 2012) mainly discuss the change of the riverbed morphology rather than the particles' suspending process interaction with the mixing layer turbulence structures and wakes of stems, which are key processes determining the concentration of nutrients, organic particles as well as sediment final deposition. The current study focusses on the dispersion process of the suspended particles in a turbulent mixing layer produced by a bankside vegetation patch.

The study on short-time sediment transport events, i.e., the instantaneous interactions between the particles and 3-dimensional turbulent structures generated by the riparian vegetation is quite limited. This may be due to challenges imposed by physical experiments and numerical simulations. It is computationally and experimentally expensive to track millions of tiny particles' motion in a complex geometry flow field while visualizing turbulent structures in a flume. Thus, previous experiments (Wang et al., 2016, Lu, 2008) only focused on the relationship between a space-averaged concentration distribution to the time-averaged flow field. They ignored the instantaneous turbulent information, and thus have provided insufficient data to unveil the nature of sediment-turbulent-plants interaction. In current study, as supported by UK Turbulent Consortium, the national Tier1 High Performance Computer (Archer) is used to carry out computationally expensive but high-fidelity simulations, in order to resolve the instantaneous turbulent flow field generated by bankside vegetation stems and track the motions of $3\text{x}10^5 \sim 5\text{x}10^5$ particles within it.

As for the numerical studies, the transportation of sediment can be modelled either in a Lagrangian method or an Eulerian method, while the flow field is computed by the Eulerian method. Most previous studies (Cheng et al., 2013, Lopez and Garcia, 1997) adopted an Eulerian method that treated particles as concentration passive scalar and described the motion of particle groups using concentration convection-diffusion equation. As proved by Graf and Cellino (2002), this method can work well for fine sediment (Stk<<1) but introduce errors for coarse-grain (or tiny-grain with Stk>1) dispersion prediction mainly because of neglecting the time lag of particles following the flow (Zhong et al., 2015). The study of Hu et al., (2002) employing Lagrangian method demonstrated the significant effects of Stk on particles dispersion in a 2-D mixing layer. Also, the determination of the sediment diffusion coefficient in this equation is problematic. Although the effect of time lag between particles and flow velocities can be modelled using an additional equation (Pilou et al., 2013), previous sandy flow studies usually assume that the sediment diffusion coefficient equals to the turbulent eddy diffusion coefficient, which means the motion of particles exactly follows the flow, but this assumption is inaccurate as tested by Graf and Cellino (2002). The simplified 1-dimensional concentration convection-diffusion equation is widely used in the vertical concentration profile prediction (Huai et al., 2020, Li et al., 2018, Lopez and Garcia, 1998), but still facing the problem of sediment diffusion coefficient selection.

By contrast, the Lagrangian method uses the discrete nature of particles, involving the effects of inertia of particles, forces exerted by flow and other particles, and some kinds of Lagrangian methods like Discrete Phase Model (DPM) and Discrete Element Model (DEM) excludes the errors induced by the diffusion coefficient selection (Sun and Xiao, 2016, De Marchis et al., 2016, Ji et al., 2014). In the present study, the DPM method without the selection of sediment diffusion coefficient is adopted to predict the sediments' dispersion in emergent plants.

Some research groups (Huai et al., 2019, Zhong et al. 2015, Fu et al. 2005) have successfully implemented Lagrangian methods for investigating vegetated sandy flows, but those studies still used a diffusion-coefficient-selection needed Lagrangian model. For example, Huai et al., (2019) adopted a stochastic Lagrangian model, i.e., Random Displacement Model (RDM) to simulate suspended sediment concentration profile over submerged canopy. Good agreement was achieved with experimental data, while the performance of that method was strongly determined by the diffusion coefficient selection. By contrast, the DPM method was used to in the current study does not require a pre-prepared determination or modelling of the diffusion coefficient. Moreover, previous studies based on Lagrangian method were mainly focused on the vertical concentration profile prediction, which still provided insufficient information on the relationship between the particles' preferential clustering and 3-demensional turbulent structures along the vegetation-side region.

However, DPM or DEM numerical simulations are computationally expensive. Hence, most of the previous DPM or DEM studies focused on the particle-laden flow in a simple geometry or a low number of particles (Oh and Tsai, 2018, Sun and Xiao, 2016, De Marchis et al., 2016, Vreman, 2015). In current study, the particle-laden flow based on the DPM was conducted in a relative complex geometry, where the grid-resolved vegetation stems occupy a large part of the channel.

Additionally, the effect of the vertical suspension effects of the VP needs further research.

Previous research observed that dense aquatic vegetation increased sedimentation as relative to the bare bed regions (Ward et al,1984, Garcia et al., 1999, Terrados and Duarte 2000, Gacia and Duarte, 2001, Agawin and Duarte, 2002). However, erosion and resuspension were observed in sparse meadows (Luhar et al, 2008, Van Katwijk et al., 2010, Lawson et al., 2012). Luhar believed that the solidity threshold indicator was around 0.1 if the drag coefficient was assumed to be 1.0 (Nepf, 2012), which could be used to categorize the vegetation patch into a sparse patch or a dense patch. For the sparse VP where the indicator value is below this threshold, the flow and stresses are enhanced to resuspend particles near the bed region. Yet, the relationship is still unclear between the density of VP and upward suspension effects in sparse VP regime.

Other findings close to the present topic are briefly reviewed here as well. The initiation of particle movement is determined by the impulse of turbulence forces. The duration of those forces is also as important as their instantaneous magnitudes (Diplas et al., 2008). Then, during the floating period, small-scale particles' clusters appear because of the centrifugal effect coming from the vortical structures in turbulent flows. These vortex structures tend to throw the heavy solid particles from the vortex cores to the interstice (Marchis et al., 2016). Moreover, turbophoresis is a key feature in a particle-laden flow, which describes particles having a tendency to migrate from higher turbulent kinetic energy location to a lower one (Caporalini et al., 1975). More recent research investigations discussing particles turbophoresis behaviour near the wall can be found in Picano et al., (2009), and Sardina et al., (2012).

In this paper, we mainly focus on fine suspended particles transport events in a straight channel with a bankside vegetation. Firstly, qualitative and quantitative relationships are investigated between particle preferential gathering locations and the transportation effects of turbulent structure. Secondly, the evolution of particle parcels in spatial and temporal space is quantitatively studied. Finally, the upward suspension (upward entrainment) effects dominated by the density of VP is discussed. The present research on the particle, turbulence and structures will provide a better understanding as relevant for the long-term morphology adaption in rivers but also for applications in chemical engineering, mining industry (Kuerten, et al., 2016) and atmospheric pollutant transport in the urban building canopy, where similar interactions can happen.

2. Methodology

The Computational Fluid Dynamics-Discrete Phase Method (CFD-DPM) method is used to resolve the flow field as well as the detailed motion history of suspended particles in the present study. CFD-DPM is based on an Eulerian-Lagrangian framework where the motion of particles is governed by Newton's second law, while the flow field is governed by the Navier-Stokes equations.

In general, the CFD-DPM method can be summarized into two main categories based on the resolutions of the particles' boundary layer, namely, the resolved method and unresolved method. As for the resolved CFD-DPM, the fluid field around each particle is resolved, even the boundary layer and wakes of the particles are captured. In contrast, the unresolved CFD-DPM considers particles as points and estimates the forces acting on particles using priori known formulae. In this paper, the unresolved CFD-DPM (two-way coupled) method was used, because the size of particles ($5\times10^{-5}\sim1\times10^{-4}$m) is smaller than the Kolmogorov scale ($1\times10^{-4}\sim5\times10^{-4}$m) in current flow conditions, the particle's near flow field is integrated into the priori known force formulae. The interactions between the flow, particles and walls are considered, but the particle-particle collision is neglected as the volume fraction of the particles is less than 0.1% of fluid volume (Crowe et al., 2011).

In previous research, CFD-DPM method has been successfully used to study particle-laden flows in a straight channel with ripple or flatbed (Elghannay and Tafti, 2017, Kuerten, et al., 2016, Ji et al., 2014, Chang and Scotti, 2003). Escauriaza and Sotiropoulos (2011) investigated the effect of horseshoe vortical structures on particles transport around a cylinder pier. Schmeeckle (2015) studied bedload transport over a backstep. However, to the best of our knowledge, no further complex geometry was studied. Some other relevant topics were also carefully discussed, including the influence of particle shapes (Zhao et al, 2015), the ratio of density between particle to flow (Durán et al., 2012), as well as the instability problems of the CFD-DPM method (Elghannay and Tafti, 2017) when the particle size is bigger than mesh sizes. All these reviewed studies indicate that CFD-DPM is appropriate for this study.

2.1 Governing equations

Computational Fluid Dynamics and Discrete Phase Method (CFD-DPM) is used to conduct these numerical experiments. The momentum transfer from the particle-phase to the fluid-phase is implemented by adding the source term in the right-hand-side of the Navier-Stokes equation. The interactions between the particle-fluid and particle-wall are considered in this multiphase system. This system is solved by the OpenFOAM CFD-DPM solver. The governing law for the fluid-phase is described by the continuity and the momentum Eqs.(1,2) including the volume fraction of the fluid-phase.

$$\frac{\partial \alpha_f}{\partial t} + \nabla \cdot (\alpha_f U_f) = 0, \tag{1}$$

$$\frac{\partial (\alpha_f U_f)}{\partial t} + \nabla \cdot \left(\alpha_f U_f U_f\right) = -\frac{1}{\rho} \nabla P - S_p + \nabla \cdot \left(\alpha_f \tau_f\right) + \alpha_f g, \tag{2}$$

where α_f, t, U_f,ρ, P, S_p, τ_f, g are the fluid phase fraction, time, fluid phase velocity, density of fluid, pressure, volumetric fluid-particle interaction force, fluid-phase viscous stress tensor and gravity, accordingly. Detailed expressions for S_p and τ_f are given in the study of Fernandes et al., (2018).

In this study, the particles are simplified as spheres, and the diameter of each particle is smaller than the fluid-phase mesh size. The motion of the particles can be categorized into translation and rotation. Those two kinds of particle motions satisfy Eqs.(3,4).

$$m_i \frac{dU_i^p}{dt} = \sum_{j=1}^{n_i^c} F_{ij}^c + \sum_{k=1}^{n_i^{nc}} F_{ik}^{nc} + F_i^f + F_i^g \,, \tag{3}$$

$$I_i \frac{d\omega_i}{dt} = \sum_{j=1}^{n_i^c} M_{ij} \,, \tag{4}$$

where U_i^p,ω_i, F_i^f, F_i^g are the translational velocity, angular velocity, particle-fluid interaction forces and gravity. F_{ij}^c and $M_{ij}$are the contact force and torque acting from object j (particle or wall) to particle i. $F_{ik}^{nc}$is the non-contact force acting on the particle i by particle k or other sources. Here we need to clarify the interactions between the fluid phase and the particle phase.

$$F_i^f = F_d + F_{\nabla p} + F_{\nabla\cdot\tau} + F_{vm} + F_B + F_{Saff} + F_{Mag} \,, \tag{5}$$

where F_d, $F_{\nabla p}$, $F_{\nabla\cdot\tau}$, F_{vm}, F_B, F_{Saff}, F_{Mag} are drag, pressure gradient, viscous forces, virtual mass forces, Basset force, Saffman force and Magnus force. The detailed expressions for each term are given in the study Fernandes et al., (2018). The drag, effective gravity, pressure gradient, Saffman force and virtual mass force are considered in this work. Other forces are neglected as little contribution of other forces to this particle system. The motion of the particles is predicted by a Lagrangian solver, governed by ordinary differential Eqs.(3-5) for the particle velocity and position update in each time step.

For the fluid solver, a finite volume method is used to discrete the governing Eqs.(1,2). The second-order backward scheme is used to march in time. Second-order upwind, *Gauss linearUpwindV*, is used for the convective terms, while second-order central difference scheme, *Gauss linear*, is used to deal with other divergence operations and gradient operations. The large eddy simulation implemented by the one-equation sub-grid model (Krajnović and Lars, 2002) deals with the turbulent effects in this multiphase problem. The PISO method is used to finish the iteration loop in each time step. The flow simulations were convergent when the residuals were smaller than 1×10^{-6} for all equations.

2.2 Mesh

The following meshes are constructed for the present simulation in Fig.1(a-c). The total number of grid points ranges from 30~40 million in different cases. The mesh is refined along the stem surfaces and the bottom of the channel, where the first grid point above the wall is at y^+=0.5 for the channel bed boundary layers. The Froude number (Fr) for these cases are defined as Eq.(6) and the values for each case are shown in Table 1. All of the cases are subcritical channel flow.

$$Fr = \frac{U_{mean}}{\sqrt{gh}} \tag{6}$$

In those cases, emergent vegetation stems are modelled as circle cylinders and the Reynolds number based on the diameter of vegetation stem (Re_d) is in the range between 1050 to 5250, which is the subcritical flow around stems with a laminar boundary layer. The definition of the Re_d is given Eq.(7).

$$\mathrm{Re}_d = \frac{U_{mean} \cdot d}{\nu}, \tag{7}$$

where Re_d, U_{mean} ,d , ν are the channel Reynolds number based on the depth of channel, average inlet velocity, diameter of a stem and kinematic viscosity of water accordingly.

Thus, the mesh resolution $d/\Delta r \geq 30$ is fine enough to capture the flow patterns (Braza et al.,1986, Yu et al., 2008). Δr and d are the first layer grid size near the stem and the diameter of stems, respectively. Mesh independence study was carried by doubling the grid points around a stem extracted from the original entire mesh. The time history of drag and lift coefficients based on those mesh are shown in Fig.2. The definitions of drag coefficient (C_d) and lift coefficient (C_l) refer to Wang et al, (2020). The time-averaged drag coefficients are 1.27 for $\Delta r/d$ = 1/30 and 1/60, which is very close to the experimental result 1.24 from Zdravkovich

(1997). To test the particle motion mesh's independence, the mesh for single particle settling test were doubled. The motion histories of the particle stayed the same.

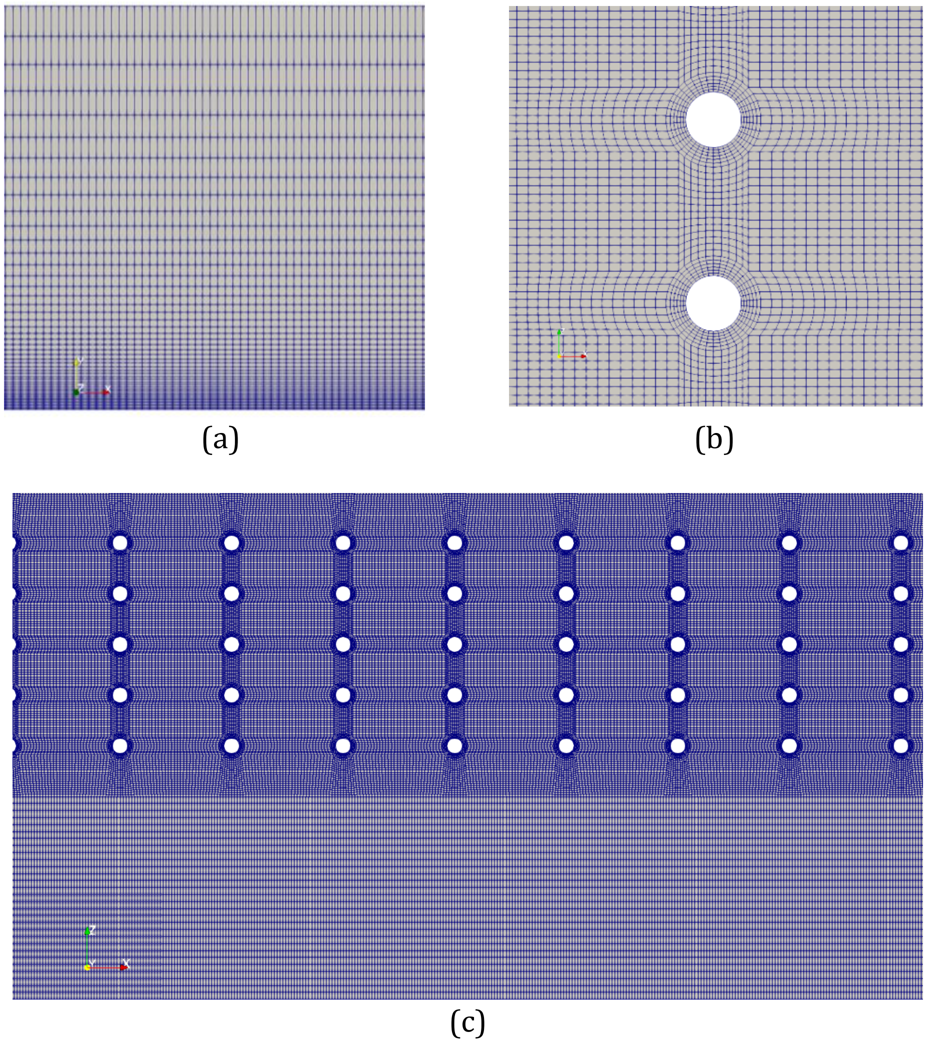

Fig.1 (a) The vertical slice of mesh; (b) The zoom-in view of the horizontal mesh around two stems; (c) The overview of the horizontal slice.

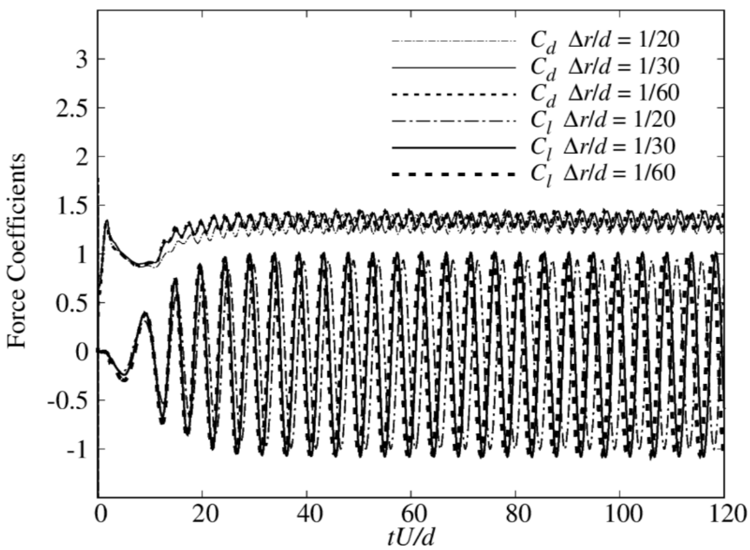

Fig.2 The mesh independence test by means of presenting drag coefficient (C_d) and lift coefficient (C_l) with $\Delta r/d$ is set as 1/20, 1/30, and 1/60.

2.3 Study cases

To investigate the particle distribution dispersed by turbulent flow along the partially vegetated channel, two groups of numerical experiments are performed. The simulations in each group consist of a case of a relatively sparse density VP, a case of a relatively dense VP and a case without VP. Attention is given to the effects of the density of the VP, where its normalised density *Dn* is given as Eq.(8)

$$Dn = \frac{V_{stems}}{V_{patch}} , \tag{8}$$

where V_{stems}, V_{patch} are the volumes of stems and the patch region, respectively. We also define Re_h as Eq.(9)

$$\mathrm{Re}_h = \frac{U_{mean} \cdot h}{\nu}, \tag{9}$$

where $\mathrm{Re}_h, U_{mean}, h, \nu$ are the channel Reynolds number based on the depth of channel, average inlet velocity, depth of channel and kinematic viscosity of water accordingly. The particles Stokes number, Stk, is defined as Eq.(10) (Chunning, et al., 2014).

$$\mathrm{Stk} = \frac{\rho_p}{9\rho_f} Re_p, \tag{10}$$

where ρ_p , ρ_f and Re_p are the density of particles, the density of each particle and Reynolds number of particles. The definition of the Re_p is provided as Eq.(11).

$$\mathrm{Re}_p = \frac{U_{mean} \cdot Ds}{\nu}, \tag{11}$$

where D_s is the diameter of a particle.

Table 1 the study cases

	Cases	Vegetation density (Dn)	Channel Reynolds number (Re_h)	Stokes number (Stk)	Froude Number	Diameter of particles
Group one	No.1	0.063	52500	9.7	0.286	100μm
	No.2	0.025	52500	9.7	0.286	100μm

	No.3	-	52500	9.7	0.286	100μm
Group two	No.4	0.063	26250	2.43	0.143	50μm
	No.5	0.025	26250	2.43	0.143	50μm
	No.6	-	26250	2.43	0.143	50μm

2.4 Boundary conditions

For the flow field boundary condition, the inlet velocity is mapped from a fully developed open channel with the same flow rate. The particles' injection at the inlet is designed as based on the Rouse law (Rouse, 1937) to mimic the natural concentration profile accounting for the particles' property and flow condition. Hence, the particle injection rate varies with height. The particles inlet flow conditions for case No.1~No.6 are plotted in Fig.3. The top of the channel is free-slip boundary condition. The side walls, bottom of channel and the surfaces of stems are assigned as no-slip boundary condition for flow. The outlet of the domain is free-stream. The particles were escaped when they passed the outlet boundary. A particle rebounds, when it collides with stems, side walls or the bottom of channel. In the current study, we assume that an elastic collision happens between the particles and vegetation stems. Normal restitution coefficient is 0.01 and friction coefficient is 0.6 when particles collide with bottom or side walls, as suggested by Sun et al, (2016) and Ji et al, (2014) because of the lubrication effects. There is no particle at the bottom of channel before releasing particles from the inlet. The time step is 5×10^{-4}s to keep the Courant Number less than 1.0.

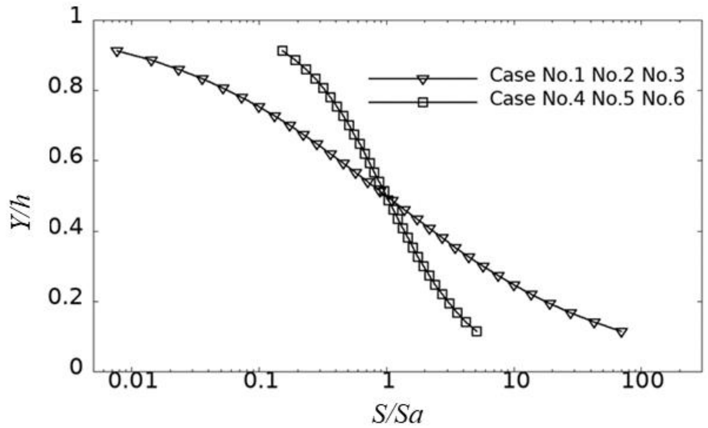

Fig.3 The particles inlet flow rate is plotted for Case No.1~No.6. S is the concentration of the particles, *Sa* is the

concentration of the *Y/h*=0.5, where the h is the depth of channel.

3. Validations and Definitions

3.1 Subregions of flow domain

The overview of subregions in the flow domain are shown in Fig.5. X Y Z corresponds to the streamwise, vertical and spanwise directions. All lengths are normalised by *Bv* (0.25m) which is the width of the VP. The size of domain is (40*Bv*, 0.6*Bv*, 2*Bv*) in the streamwise, vertical and spanwise directions, accordingly. The leading edge of the VP is set as X=0. The whole flow region is divided into several subregions based on the expected flow patterns in those regions. Previous studies have provided the length estimation formula or dividing criterion for subregions R2, R4, and R6, but regarded the whole VP as a single subregion (Huai et al, 2015, Zong and Nepf, 2011, Chen et al., 2013). In the present research, the VP region will also be divided into subregions based on the turbulent structures and particle organizations. Here, we briefly present physical descriptions for those subregions: R1 is the upstream flow of the VP, where the flow and particle distribution are span-wisely uniform in most of this region.

R2 denotes the diverging flow region where the flow leaks through the VP's side interface. In Fig.5, the length scale of the diverging flow R2, X_D, is estimated by Eq.(12) (Zong and Nepf, 2011, Chen et al., 2013).

$$\frac{X_D}{L_c} = \beta(1+\alpha C_d a h), \qquad (12)$$

where C_d is the canopy drag coefficient, and a is the frontal area per canopy volume. The scale factors α = 2.3 ± 0.2 and β= 1.5 ± 0.2 determined from a range of terrestrial and aquatic canopies, which it is defined as the ratio between the average height of plants (h) and the depth of water (Chen et al. 2013). The canopy drag length scale L_c (Belcher et al. 2003) is estimated by Eq.(13).

$$L_c = \frac{2(1-Dn)}{C_d a}, \qquad (13)$$

where Dn is the solid volume fraction of the vegetation, denoting the ratio between the vegetation volume to the vegetation patch volume.

R3 is the front part of the VP, where turbulent structures develop but are not fully developed yet and particle stripes happen. R4 is the developing region of the turbulent mixing layer. R5 is the region where the turbulent structures are fully developed in the VP, reaching a maximum of turbulence intensity, where the upward entrainment of particles occurs. The fully developed region for the mixing layer is named as R6. The identification of the fully developed region is based on the spanwise time-averaged velocity profiles and Reynold stress profiles along the streamwise direction. For example, the mixing layer is fully developed where X/*Bv*>12 in case No.1, as shown in Fig.4.

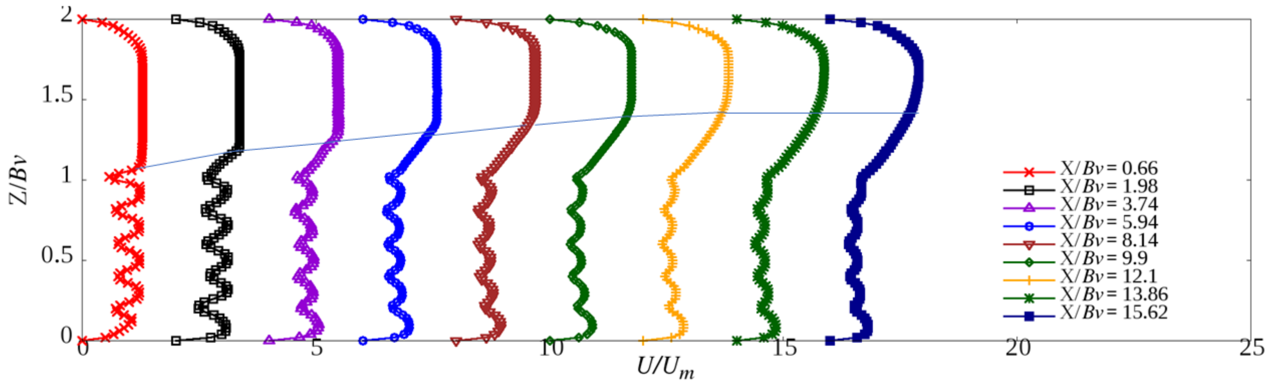

(a)

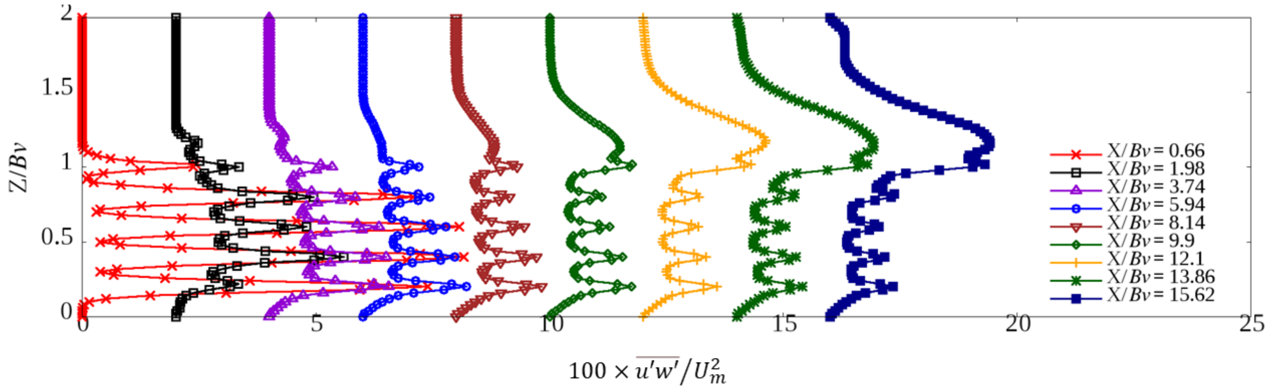

(b)

Fig.4 (a) The normalized spanwise time-averaged velocity profile in streamwise direction in case No.1. (b) The normalized spanwise time-averaged Reynolds stress in the streamwise direction in case No.1. u' is the streamwise velocity fluctuation, w' is the spanwise velocity fluctuation.

The turbulence structures gradually attenuate in R7 region because of a velocity reduction, where the vertical entrainment of particles is nearly in equilibrium with deposition, as identified by Fig.29. R8 is assigned as the wake region of VP. Note that the length scale of each region varies and may even disappear depending on the inlet flow conditions (i.e., the channel Reynolds number, Re_h), vegetation density (Dn), and the length scale of VP. In some cases, the transition between the different subregions is slow and the boundaries between them are blurred. Identifications of subregions are summarized in Table 2.

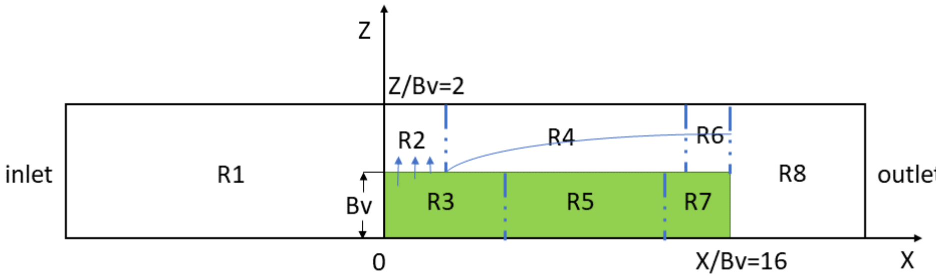

Fig.5 the overview of schematic of subregions of the partially vegetated channel.

Table 2 A summary of subregions.

Region	Region identification or length scale estimation
R1	The upstream flow region of the VP
R2	The diverging flow region, the streamwise length is estimated by Eq.(12) (Zong and Nepf, 2011, Chen et al., 2013)
R3	The front part of the VP, the streamwise length scale is identified by particle stripes length scale, as shown in Fig.9 .
R4	The developing mixing layer region, the region is identified by the spanwise velocity profile and Reynolds stress profile, as shown in Fig.3
R5	The particle vertical entrainment region, the upward entrainment of particles occurs in this region.
R6	The fully developed region for the mixing layer. This region is identified by the spanwise time-averaged velocity profiles and Reynold stress profiles along the streamwise direction.
R7	The vertical particle concentration profile nearly fully developed, as shown in Fig.29.
R8	The wake region of vegetation patch.

3.2 Validations

The simulation results have been assessed for the fluid-phase and the particle-phase. The flow field (Case No.5 listed in Table 1) is compared to the experimental data from Huai (2015), the vertical average velocity profile along the spanwise located in X/*Bv*=14 is shown in Fig.6. Good agreement between the numerical results and experimental results has been achieved. The particle's settling velocity in a still water circumstance has been assessed as well. A wide range of particle diameters, from 50μm to 600 μm, has been tested, which validation range covers the present numerical particle sizes. As revealed in Fig.7, the particle settling velocities reach steady values after the acceleration stage, and these steady settling velocities are perfectly consistent with published analytical and experimental data in the literature.

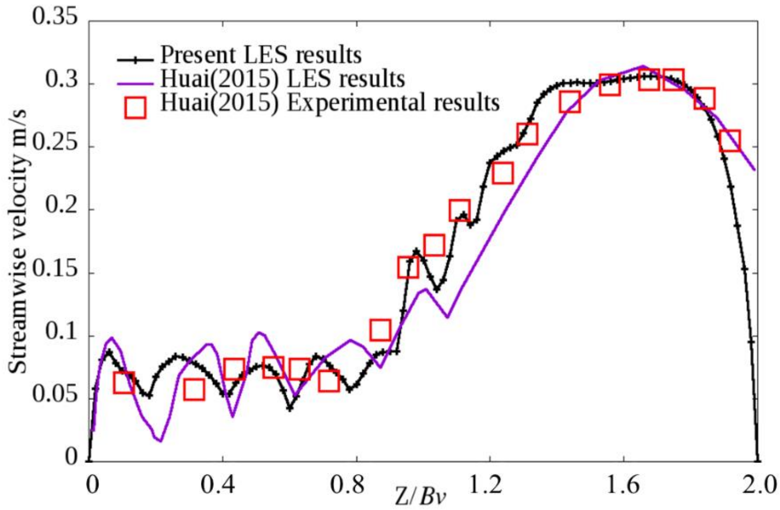

Fig.6 the validation of time-vertical-averaged velocity profile along the spanwise in X/*Bv*=14

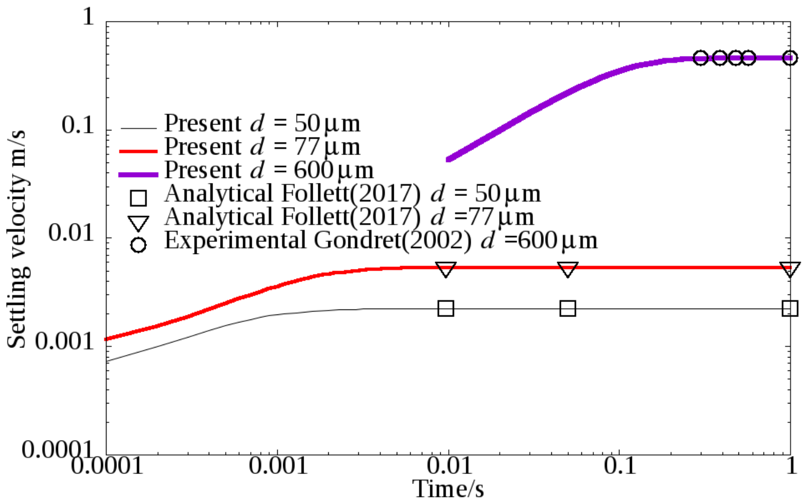

Fig.7 the validation of the particle settling velocity in still water

To validate the prediction of the suspended sediment and turbulent flow, the vertical space-averaged concentration profile in the region R7 (R7 is introduced in the next section 3.2) is compared to the experimental results with similar flow condition, vegetation density and particle properties. The details of the experimental conditions of Lu (2008) are shown in Table 3.

Table 3 the experimental conditions of Lu (2008), the defination of those demonsionless parameters in this table are present in the next section.

Cases	Vegetation density (Dn)	Channel Reynolds number (Re_h)	Stokes number (Stk)	Diameter of particles
D12-2	0.0141	35016	7.6	110~310μm
D12-3	0.0283	35016	4.4	110~310μm
D15-3	0.0283	43770	4.4	110~310μm
D18-3	0.0283	52524	4.4	110~310μm

As shown in Fig.8, the numerical prediction agrees well with the experimental data trend, the discrepancy between the results is from the difference between the multiphase system conditions. This comparison indicates the reliability of the present simulation cases.

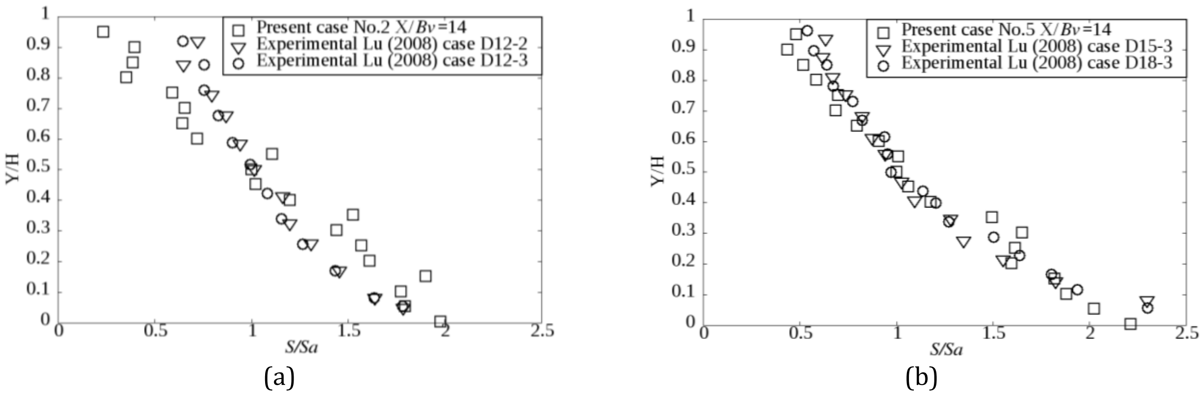

Fig.8 the validation of the verticle suspended sendiment profile in the downstream end of VP (region R7 marked in Fig.5) The experimental data are from Lu (2008).

3.3 Identifications of target state of the simulation

One necessary identification of target state occurring in time is that the particle growth rate in the entire domain remains almost constant, which means that after a long time of particle injections, the difference between the number of particles injected from the entrance of the channel and the particles escaping from the outlet of the channel becomes nearly constant in time.

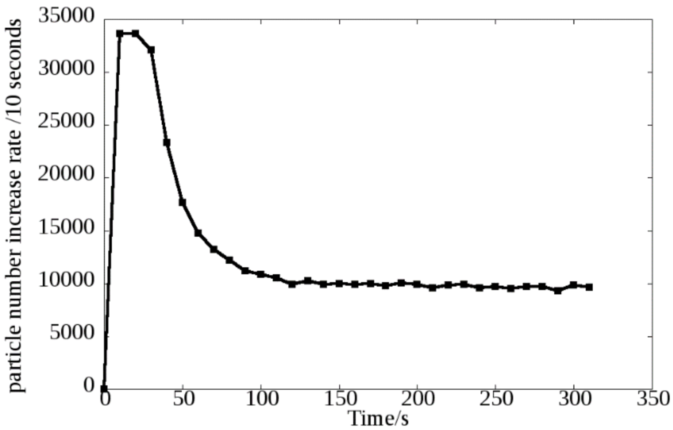

Fig.9 The particle number increase rate per 10 seconds in the whole domain in case No.1. We define the target state as the period after 100s in this case.

The present simulation cases are similar to the study of Huai et al., (2015). Huai et al. pointed out that after the time (t>3T=3L/U_{mean}) the flow reached fully developed state. In the present cases, the initial state is mapped from a fully developed non-vegetated channel, and then the 6T was simulated for all cases to reach fully developed state before releasing the particles. Take case No.1 as an example, particles are not released before the flow is fully developed in the whole region. As displayed by Fig.9, the particles start to be released at t=0s, and then fills the entire area continuously until the end of the simulation. As a result, the total number of particles in the domain experiences a high increment during 0-40s since no escape event happens. However, after the 40s, particles escape from the outlet boundary, so the particles net growth rate drops gradually. Nevertheless, after a considerable period (more than 100s), the growth rate of particles in the entire domain stays at a low level but does not drop to zero. This is due to the net deposition of some particles at the channel bed because of the obstruction of vegetation. Therefore, we define this period as the research target state. This is because during this state, the bedload increases results from a steady deposition rate. However, the statistics of suspended particles' concentration stay nearly stable in time, and the present study only focuses on the suspended sediment.

The other necessary identification of target state is that the Relative Stable Test (RST) index keeps the statistically unchanged in the target state. As shown in Fig.10, the RSTs of vegetated cases are less than 15%, while RSTs of non-vegetated cases are less than 6%, where the RST for the moment t_i is given by Eq.(14).

$$RST\Big|_{t=t_i} = \frac{1}{N}\sum_{k=1}^{N}\left|\frac{f(z_i)-\overline{f(z_i)}}{\overline{f(z_i)}}\right|\Bigg|_{t=t_i} . \qquad (14)$$

Where N is the sample number of a spanwise (Z) probability density function (PDF). The PDF at a spanwise location $z=z_i$ is given as $f(z_i)$. The time-averaged of PDF is $\overline{f(z_i)}$. The detailed definition of PDF is given at section 4.2.1.

The physical meaning of RST is the degree of the difference between the instantaneous PDF to the time-averaged PDF. Although the total number of particles are increasing in the domain, the PDF of the spanwise distribution is statistically stable along the time scale of particles' deposition. This is a while the change of the channel morphology due to the deposition is much longer than the deposition time of particles. We can estimate the time that the deposition of particles occupies 1% of the whole domain volume is over o(10^5) seconds based on the current conditions and assumption. The release rate is 3000~4000 particles/second at the inlet. The volume of each particle is o(10^{-12}) m^3. We very conservatively assume all the particles deposit in the channel bed before leaving the domain. As shown in Fig.10, the RSTs indicate that the statistics practically stay unchanged during 150s~200s for cases No.1~3 and 350s~400s for cases No.4~6, which is far less than o(10^5) seconds. Therefore, the morphology modification of the channel bed owing to the sediment deposition is not considered in the present study.

Hence, as shown in Fig.10, the increase number of particles in the domain does not effectively influence the PDF in the investigated period. Therefore, we select this period as the research target state.

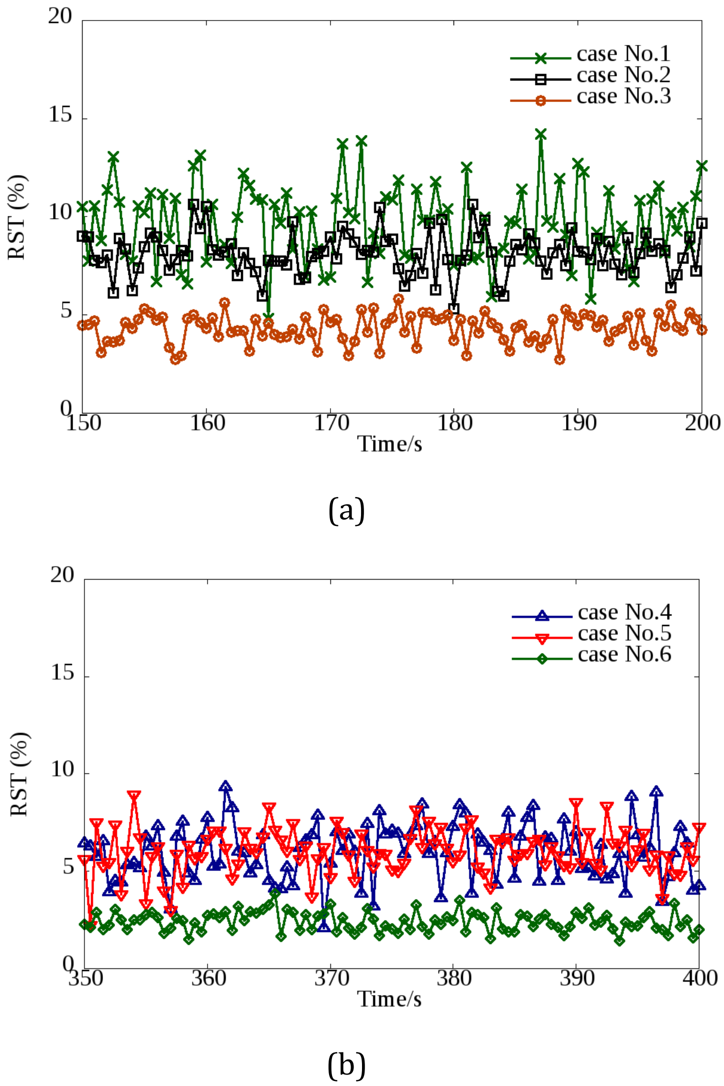

Fig.10 The relative stable test (RST) which is plotted along time where (a) is the RST for group one and (b) is the RST for group two. The sample location is (14≤X/*Bv*≤16 and 0<Z/*Bv*<2).

4. Results and discussions

4.1 The relationship between the turbulent flow patterns and particle distribution

The redistribution of particles in the partially vegetated region is of high interest as compared to previous studies which usually modelled the concentration of suspended sediment as passive scaler without a delayed temporal response to turbulent flow structures. The results of the present study show that the particles are uniformly distributed in the spanwise direction when they are located in the upstream of the vegetated region. However, an escaping behaviour of particles occurs in the region of intense vortices along the VP side. Those vortices structures are visualized by Q-criterion and vorticity separately in the following sections. The definition of Q-criterion in current flow condition (incompressible flow) is given in Eq.(15) (Banko and Eaton, 2019).

$$Q = -\frac{1}{2}(\nabla u : \nabla u^T), \quad (15)$$

where u is velocity vector. T is the transpose operation of a matrix. The Q-criterion have been used to visualize important vortical structures in these partially vegetated channels. The relationships between the vortices to particles distribution in a partially vegetated channel are firstly presented as follows.

4.1.1 The relationship between the Q-criterion and particle distribution

For the clarity of flow pattern and particles' location, Fig.11 (a)(b) present the top view of turbulent structures and particles separately in the entire vertical domain. The turbulent structures are visualized by Q-criterion ($Q=25s^{-2}$) and coloured by green or dark shade, while the particles are coloured by their instantaneous velocity magnitude (t=200s and t=400s for cases No.1~3 and cases No.4~6, respectively). In the inner space of the VP, the turbulent structures are generated at the leading row of stems, having the length scale of the stem's diameter at the beginning, and keep developing in the wakes of stems in region R3, as shown in Fig.12. Those flow structures among the stems play an important role in upward entrainment of the sediment in VP, which will be discussed later. In the non-vegetated outer regions (R2, R4), the turbulent flow structures develop along the interface between VP and non-vegetated region (R4). Their scales grow from the stems' scale into the patch's scales. Those turbulent structures are fully developed in region (R6) where the spanwise distribution is highly uneven, but on the other hand, the streamwise distribution tends to be uniform.

These large-scale structures have a pronounced effect on the distribution of particles. As seen the mixing layer region (R6) is occupied by the larger size of turbulent structures in the zone with much less particles. This is because Stk>1, and the strong curl streamlines in the vortex's region. Thus, the centrifugal effects of the vortex core “throw away” those particles to the periphery of vortices.

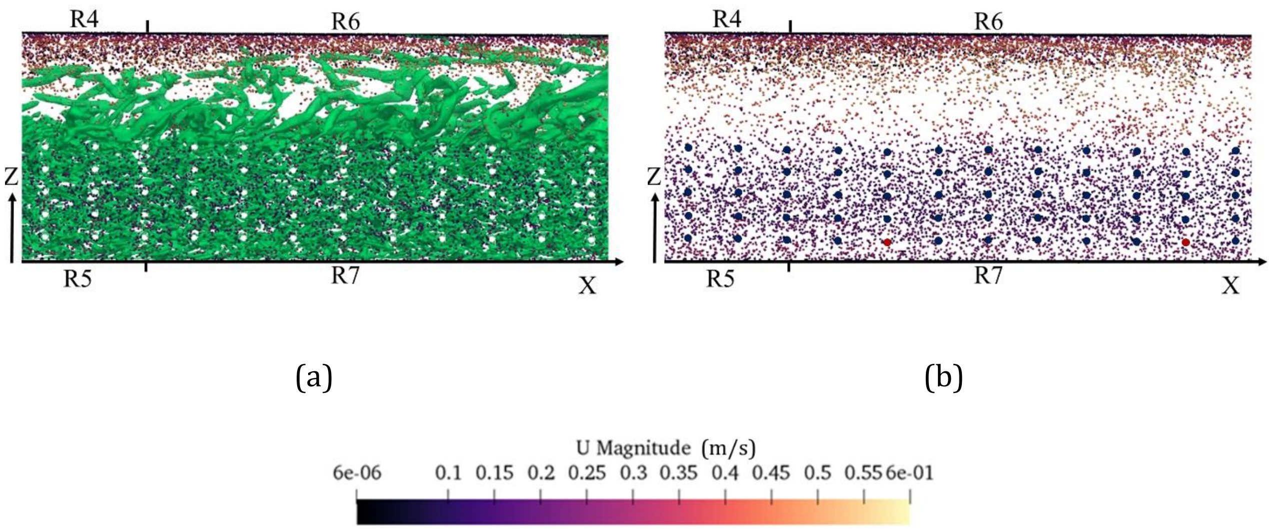

Fig.11 (a) the top view of a zoom-in distribution of particles in the vertical regions R6 and R7 with turbulent structures visualized by Q-criterion ($Q=25s^{-2}$). (b) the presence of particle distribution in the whole vertical domain while hiding the turbulent structures of Fig.11(a). The colour bar denotes the instantaneous velocity magnitude of particles (t=200s). For clarity, the circles/points are the particles which is 100 times bigger than its real size.

As shown in Fig.12(a)(b), a comparison is made between Cases No.1 and No.2 to illustrate the effects of *Dn* on the turbulent structure development and particles' distribution. The other comparison was also made for Case No.4 and case No.5. All those comparisons indicate that relatively dense VP (Cases No.1 and No.4) generates more intensive turbulent structures in the VP region. Those turbulent structures act as a powerful carrier to redistribute particles span-wisely. Specifically, a big difference can be observed for the front part VP region (R3). For the dense cases, the intensive turbulent structures are generated immediately when the flow passes through, and the wake structures are observed. In contrast, for the sparse cases (Case No.2, No.5), the leading rows of stems and the side stems generate much less turbulent structures.

Furthermore, the distribution of particles is different in the region R3. What stands out is the particle stripes gathered in the gaps between the stems in the R3 region in sparse cases, as displayed in Fig.12(b)(d) (the Fig.15 in the following section also presents the scenario discussed above in the near-bed region). However, for the dense cases shown in Fig.12(a)(c), there are weak stripes of particles between the stem gaps in the R3 region. This is because the stem diameter in Case No.1 is larger than that of Case No.2. Thus, the length scales of the stem wakes in Case No.1 are larger than that of Case No.2 and have a stronger mixing capability for the particles' spanwise motion.

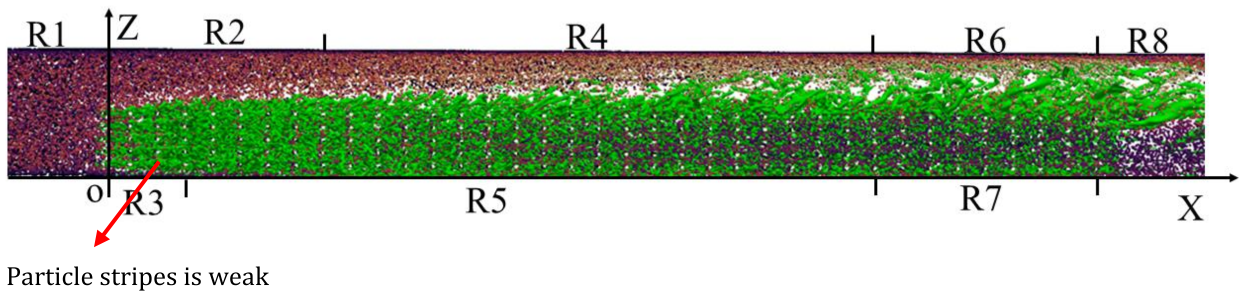

(a) (case No.1 Q=25s-2)

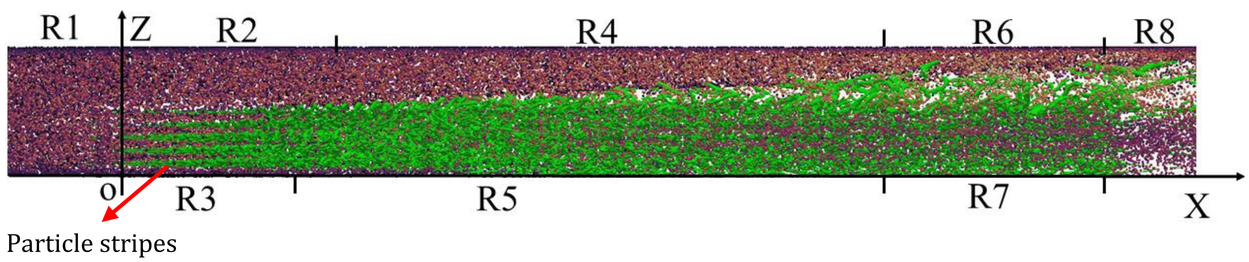

(b) (case No.2 Q=25s-2)

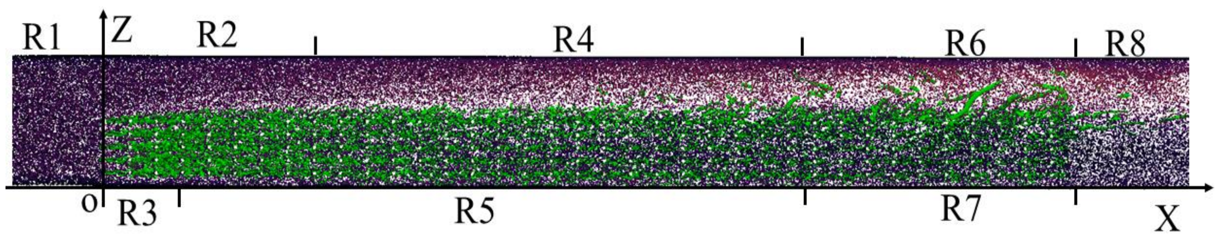

(c) (Case No.4 Q=25s-2)

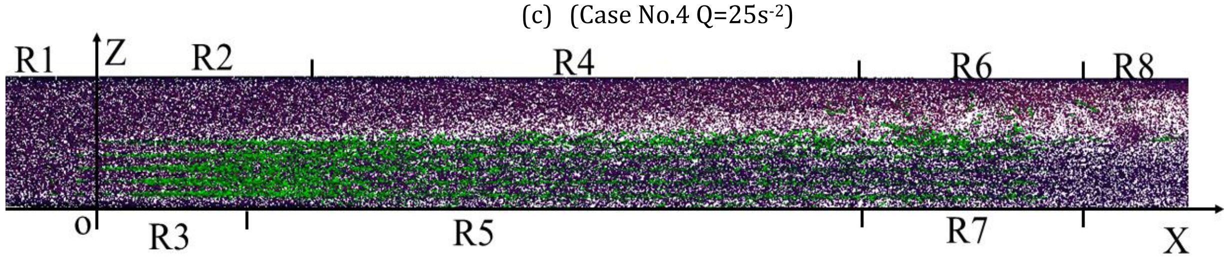

(d) Case No.5 Q=25s-2)

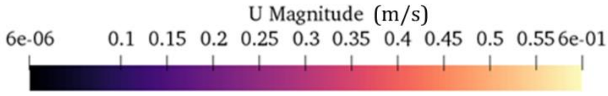

Fig.12 the overview of the particle distribution and turbulent structures in the vertical domain visualized by Q-criterion. The particles are coloured by the instantaneous velocity magnitude (t=200 for case No.1 and No.2, t=400 for case No.4 and case No.5). (a~d) present the case No.1, case No.2, case No.4, case No.5, respectively. For clarity, the circles/points are the particles which is 100 times bigger than its real size.

The particles' stripes length scales are determined by the vortex structures development in the VP regions. As mentioned, the upstream part of the patch region R3 is not the region occupied by rich turbulent structures in the sparse cases of No.2, No.5, though the flow velocity in R3 is higher than in the R5, R7 regions of the VP. The interesting observations are that the particles stripes stretch along the entire growing region (R3) in both sparse cases and begin to disperse only in the most intensive turbulent region (R5). However, for the dense Cases No.1, No.3, the stronger blockage effects highly reduce the length of growing region (R3) and stripes of particles are hard to be observed. Thus, we conclude that the stripes of particles in the upstream region of the VP are governed by the *Dn* or the initiation turbulent length scale, i.e., the stem diameter size.

4.1.2 The relationship between the vertical vorticity and particle distribution

Apart from the close relationship between flow patterns and particle organization visualized by Q-criterion, a highly surprising finding is that the distribution of particles perfectly coincides with the vertical vorticity distribution, especially in near channel bottom region. To demonstrate this finding, the instantaneous flow domain is sliced by horizontal planes through the VP and suspended particles in various heights where the contours of the vertical vorticity component are presented.

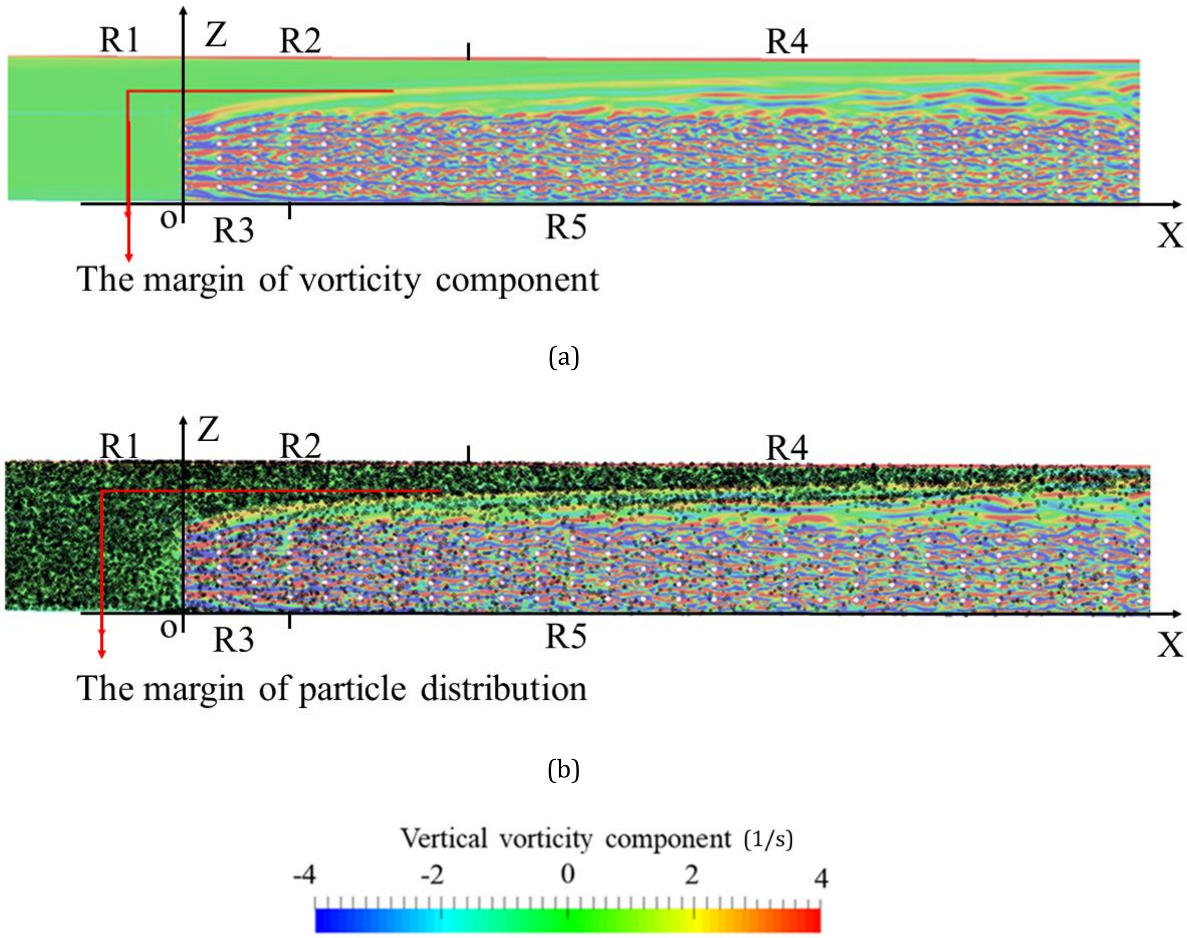

Fig.13 (a) the vorticity distribution contour while hiding the particles in this slice. (b) the presentation of particle distribution and the vertical vorticity distribution in the height Y/D_p=5. For clarity, the circles/points are the particles which is 100 times bigger than its real size.

Fig.13(a) presents the instantaneous horizontal contour slice of vorticity in Y/D_p=5. Fig.13(b) shows the particle distributions in this slice. What stands out is that the visible margin of particles in the non-vegetated region matches the vorticity contour surface (vorticity=2s^{-1}), which is illustrated by the marked line developing from the leading edge. These two pictures clearly demonstrate that the particles preferential concentration is strongly governed by the vorticity distribution in the near-bottom region. This finding was also observed in other cases, like case No.2 shown in Fig.15. It is a good open research question that try to find a qualitative relationship between this vorticity value to the vegetation and flow parameters such as *d*, *Dn*, and Re_h in future study.

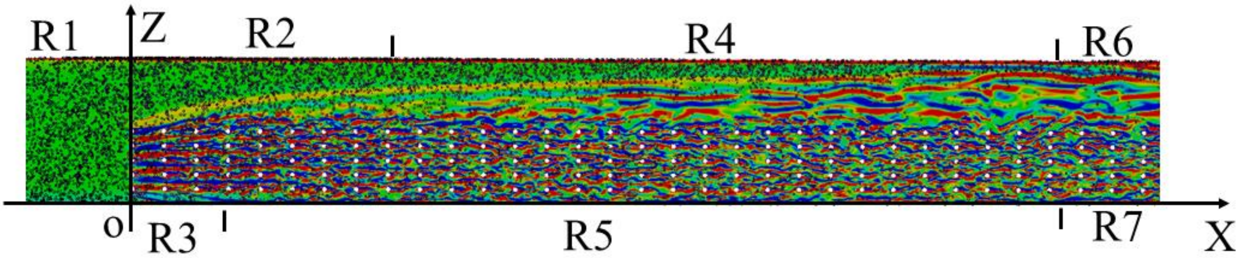

(a) Y/D_p=50

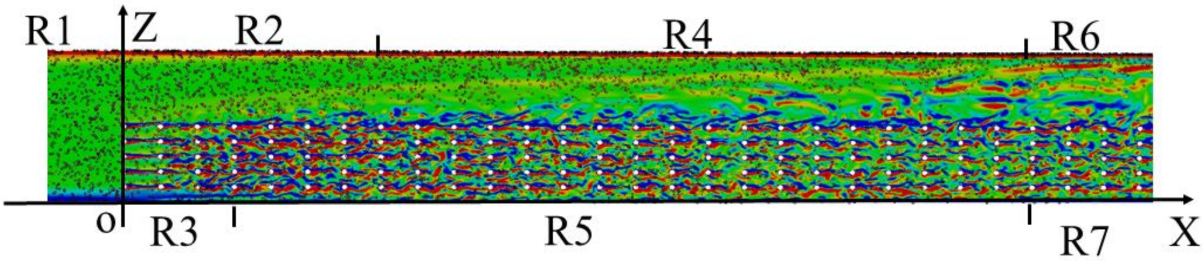

(b) Y/D_p=200

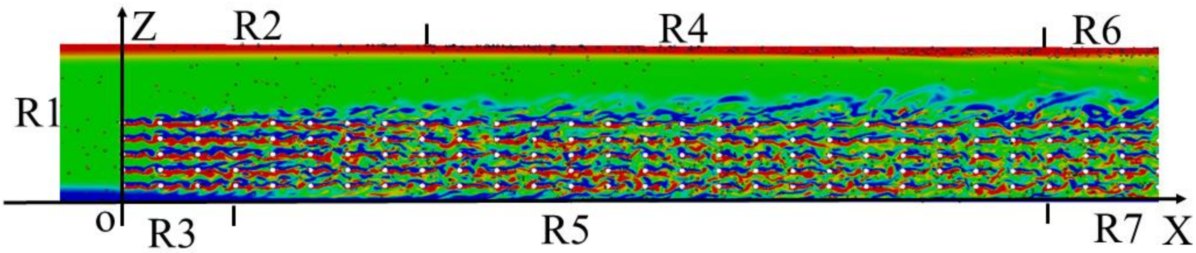

(c) Y/D_p=500

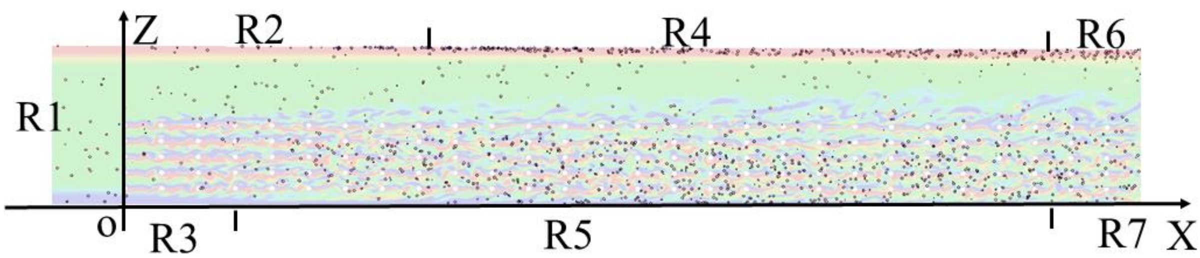

(d) Y/D_p=500

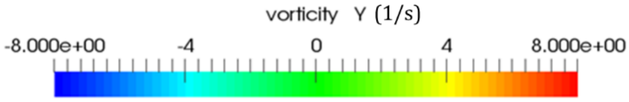

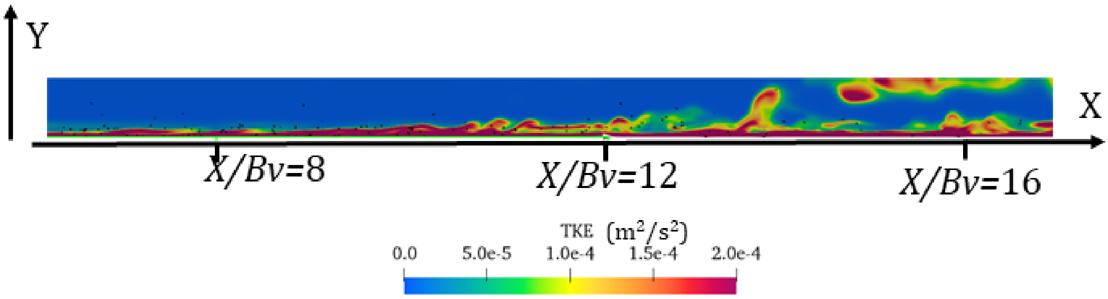

(e) The contour plot of TKE on the vertical slice parallel to the side wall. (Z/Bv=1.6)

Fig.14 (a)(b)(c) are the relationship of particle distribution and the vertical vorticity distribution in various height in case No.1. (d) highlights the particles distribution by setting the vorticity contour (c) as transparent. For clarity, the circles/points are the particles which is 100 times bigger than its real size. (e) The contour plot of TKE on the vertical slice parallel to the side wall (Z/Bv=1.6).

Fig.14(a)(b)(d) indicates that the margin of the particle distribution becomes blurred and does not exactly match the vertical vorticity component distribution, as the slice location rises over Y/D_p=30. Nevertheless, the particles concentration is still low inside the mixing layer due to its vortices. This gradual discrepancy of margin of particles and vorticity can be attributed to the turbulent structures developing from the channel bottom. As the slice moves away from the channel bed, the particles are not only transported by the vorticity in the horizontal plane but are also affected by the turbulent structures generating from the channel bed, as shown in Fig. 14(e).

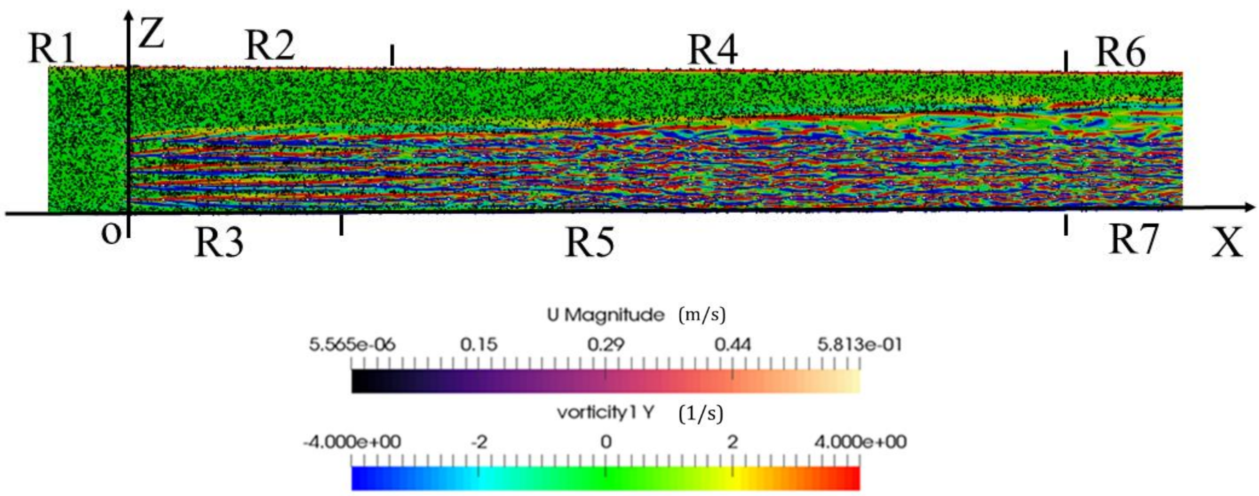

Fig.15 the relationship of particle distribution and the vertical vorticity distribution in height Y/D_p=5 in case No.2. For clarity, the circles/points are the particles which is 100 times bigger than its real size.

Overall, the particles tend to stay in a lower vorticity region in all cases. Comparing the vorticity distribution between the dense and sparse cases, the vorticity is strongly affected by the density of VP. As shown in Fig.15 of the sparse Case No.2, there is no clear vorticity edge developing from the leading edge until the end of the diverging flow region (R2, X/*Bv*=4). Thus, the particles nearly uniformly suspend or deposit in region R2, and no clear segregation happens. At the developing region (R4) a thinner edge transports the particles as compared to the dense Case No.1 in Fig.13. In the developed region (R6), the distribution of particles still follows the edges of the maximum magnitude vorticity, which is consistent with the dense cases.

4.2 Statistics of particle distribution

To quantify the statistics of particle distribution a Probability Density Function (PDF) and the variance of PDF are studied to unveil their physics characteristics.

4.2.1 Probability density function of particles distribution in spanwise

For a streamwise region of [*x*, *x*+2*Bv*], the spanwise domain $z \in [0, 2Bv]$ is uniformly divided into *M* subregions that are numbered from 1 to *M*. For the i_{th} subregion, the spanwise coordinate in is $[z_i - \frac{Bv}{M}, z_i + \frac{Bv}{M}]$ where z_i is defined by Eq.(16). The definition of Probability Density Function (PDF) in the i_{th} subregion is Eq.(17).

$$z_i = (2i-1)\frac{Bv}{M}, \tag{16}$$

$$f(z_i) = \frac{\overline{N}_i}{\sum_{i=1}^{M} \overline{N}_i}, \tag{17}$$

where *Bv* is the spanwise length scale of the VP, $\overline{N}_i$ is the time-averaged number of particles in the i_{th} subregion. f denotes the PDF.

Case No.1 is chosen to show the overview of the variations of PDF along the streamwise direction, as shown in Fig.16(a). Owing to the presence of VP, the spanwise (Z) uniformly distributed particles, in region R1, are transported span-wisely during the growth of the vortices in the mixing layer along the VP region in the streamwise direction (0≤X/*Bv*≤16), while the spanwise non-uniformity reduces after the end of the VP region (X/*Bv*≥16). By contrast, the PDFs stay relatively uniform in the spanwise and streamwise directions in Case No.3 because of no mixing layer was produced by the vegetation patch, as displayed in Fig.16(b).

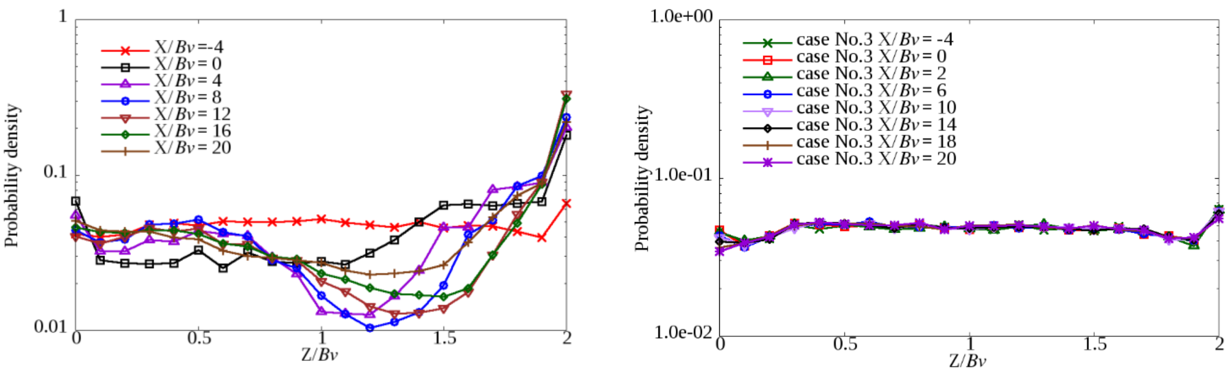

(a) Case No.1 (b) Case No.3

Fig.16 (a)Probability density function (PDF) in spanwise (Z) located in different streamwise location (X) in case No.1. Note that 0<Z/*Bv* <1 is vegetated region, while 1< Z/*Bv*<2 is non-vegetated region. (b)Probability density function (PDF) in spanwise (Z) located in different streamwise location (X) in Case No.3.

To study the effects of *Dn* on the PDF in different subregions, all vegetated cases are compared. As shown in Fig.16, in the near upstream region of VP (-4≤X/*Bv*≤0, R1), the flow velocity gradually decreases, but the distribution of particles is relatively less affected by the flow slowing down. The spikes of the PDF on the two side walls, where there is an obvious the preferential wall accumulation i.e., increase of PDF in (Z/*Bv*=2) than Z/*Bv*=0, can be explained by the coherent sweep and ejection events (Marchis et al., 2016) and spanwise flow, caused by the VP obstruction in near downstream. Moreover, two troughs in the vicinity of the two side walls (Z/*Bv*=0.2 and 1.8) can be seen almost in all cases owing to the small scale of vortices generated by boundary layer of the walls and turbophoresis (Picano et al., 2009, and Sardina et al., 2012).

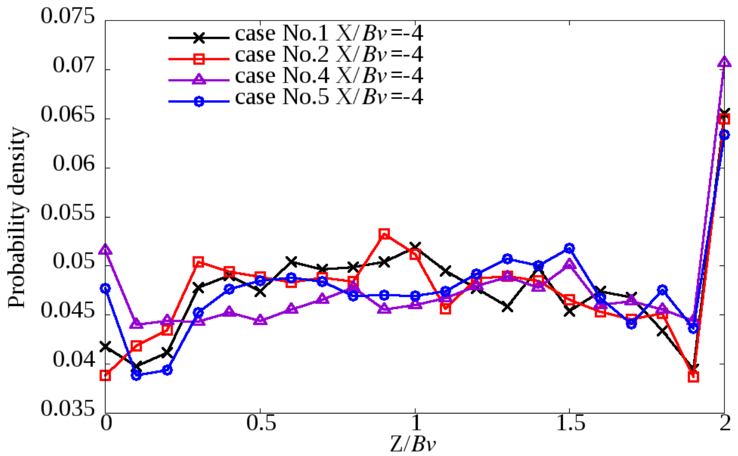

Fig.17 Probability density functions in spanwise (Z) located in region R1 (X/*Bv* =-4) in case No.1, case No.2, case No.4 and case No.5.

(i) The diverging flow region, 0≤X/*Bv*≤4

In this region, the diverging flow in region R2 and the particles' 'wiggles' in region R3 are the main features. In the diverging flow location, the non-vegetated region R2 (1≤Z/*Bv*≤2) has higher PDF, as compared to the vegetated region R3 (0≤Z/*Bv*≤1). This is because of the sudden obstruction of the flow leading to a strong diverging flow and the flow bypassing the leading edge of the VP (Huai et al. 2015). The diverging flow and the bypass flow transport particles to the region R2 which region is of less flow resistance and thus experiences a higher velocity.

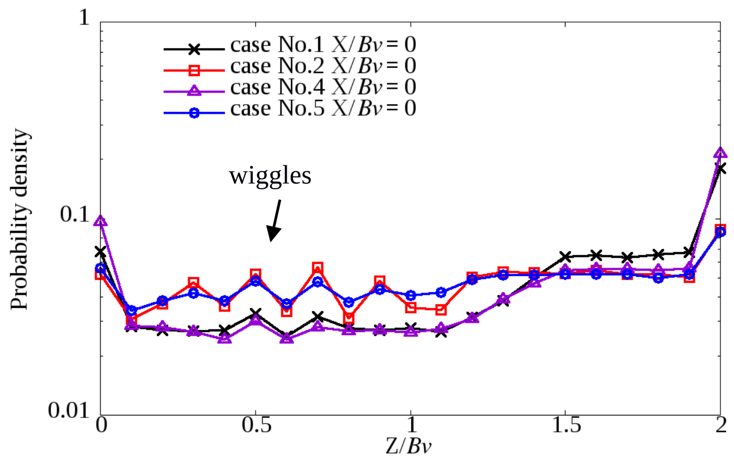

Fig.18 Probability density in spanwise (Z) located in region R2 and R3 (X=0) in case No.1, case No.2, case No.4 and case No.5.

As revealed in Fig.18, the PDF of all vegetated cases collapse into two groups in this leading-edge region (R2, R3, 0≤X≤2*Bv*), which implies that the density of the VP may have a more important role than the Reynolds number of the channel flow (Re_h) and the Stokes number of the particles (Stk), detailed in Table 1, on the distribution of particles in current variables' space. Generally, the cases with dense *Dn* (cases No.1, No.4), have a stronger diverging flow, generating as twice the PDF than that of the sparse cases in the VP region. However, for the sparse cases (cases No.2 and No.5) the flow penetration is stronger in VP, thus this PD's increase is quite mild near the walls.

Moreover, for the sparse cases, stronger 'wiggles' of PDF in the VP region are presented, as the contrast with those of the dense VP cases. The 'wiggles' of the PDF are the numerical interpretation of the phenomenon that the particles are accumulated as stripes when penetrating the leading edge of VP as shown in Fig.12(b)(d) and Fig.15. These 'wiggles' of the particles stripes happen in all cases but are extremely obvious in case No.2, which indicates that the relatively sparse *Dn* and higher Re_h facilitate this phenomenon of particles flowing through the stem gaps but are not dispersed by the wakes of the stems. On the other hand, in dense cases this wake dispersion effect is much stronger, leading to weak 'wiggles' in this region.

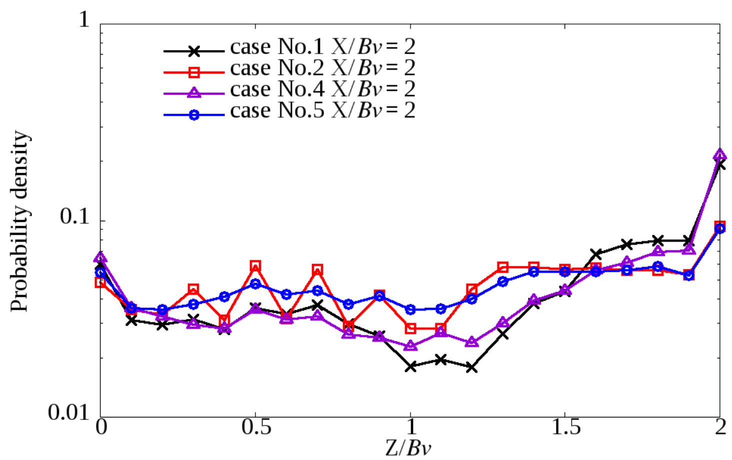

Fig.19 Probability density in spanwise (Z) located in region R2 and R3 (X/*Bv*=2) in case No.1, case No.2, case No.4 and case No.5.

When particles flow into the 2≤X/*Bv*≤4 streamwise region, the PDF for all cases in the mixing layer (1≤Z/*Bv*≤1.5) of the non-vegetated region (1≤Z/*Bv*≤2) begin to decrease, especially for Cases No.1 and No.4, with the dense VP. This is because the velocity difference of the shear layer is relatively larger than in the cases of sparse VP, leading to the growth of vortices to a stronger extent in the same streamwise location. It is also worth noting that there has been a marked PDF drop in the mixing layer region of Case No.1 which has a larger Re_h, in the denser VP.

On the other hand, in the vegetated region (0≤Z/*Bv*≤1) the strength of these 'wiggles' reduce in Case No1, No.4 and No.5 but keeps the same or even of higher level for case No.2. Thus, we can believe that the streamwise length scale of the particle stripes in streamwise is inversely correlated to *Dn*.

(ii) The mixing layer developing region, 6≤X/*Bv*≤12

The mixing layer's gradual development is a key feature in region R4, where the mixing layer thickness grows along with the development of turbulent structures and vortices region. As discussed above, the distribution of the particles is dominated by the vortices' locations. As shown in Fig.20(a)(b) of all cases the lowest point of the PDF moves away from the interface (Z/*Bv*=1) of VP, where particles are transported downstream in the developing region. These statistical results are caused by the high vorticity region becoming wider and the Q-criterion structures of vegetation patch size developing span-wisely as displayed in Fig.12.

Moreover, the effects of the *Dn* result in a velocity difference between the vegetation region and the non-vegetated region, thus affecting the intensity of the vorticity in the mixing layer region. Therefore, comparing the PDF of the same location between the dense cases to sparse cases respectively, all dense cases show more highly non-uniform distributions. PDF_{max}-PDF_{min} for *Dn*=0.063 cases is around 0.19 in both cases No.1 and No.4, while the PDF_{max}-PDF_{min} for *Dn*=0.025 cases is 0.07 for case No.2 and 0.085 for case No.5.

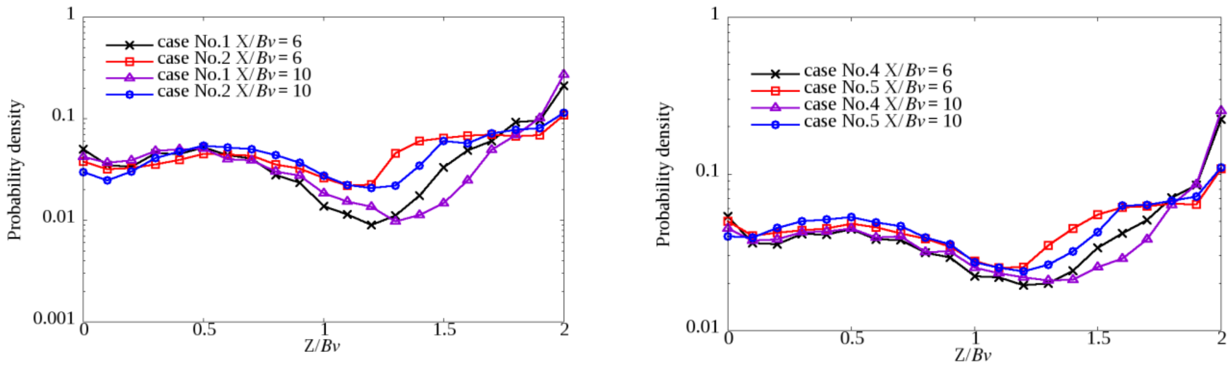

(a) (b)

Fig.20 (a) Probability density functions in spanwise (Z) located in region R4 and R5 (X=1.5 and 2.5) in case No.1 and case No.2; (b) Probability density functions in spanwise (Z) located in region R4 and R5 (X=1.5 and 2.5) case No.4 and case No.5.

(iii) The mixing layer fully developed region, 14≤X/*Bv*≤16

The key feature in this region (R6) is that the mixing layers are fully developed for the dense cases, and almost fully developed for the sparse cases. As expected, there is no much variation in the time-averaged PDF along the different stream-wise locations for each case, as seen in Fig.21.

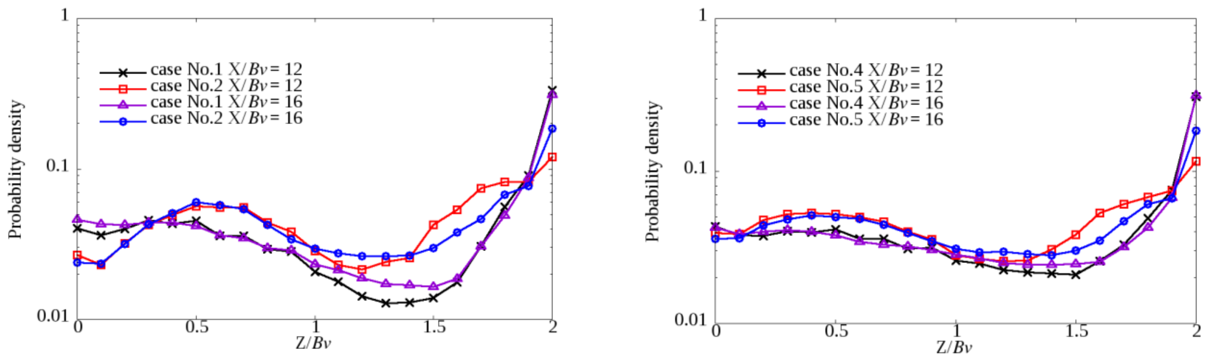

(a) (b)

Fig.21 (a) Probability density functions in spanwise (Z) located in region R6 and R7 (12≤X/*Bv*≤16) in case No.1 and case No.2; (b) Probability density functions in spanwise (Z) located in region R6 and R7 (12≤X/*Bv*≤16) case No.4 and case No.5.

It is very clear that the *Dn* determines the final characteristics of the PDF in the fully developed region. For the relatively dense patch cases, *Dn*=0.063, the lowest value of PDF is at Z/*Bv*=1.5, which is the middle of the non-vegetation region. By contrast, the minimum PDF stays at Z/*Bv*≈1.2 in the sparse cases, which is closer to the VP interface. This difference owes to the variation in the turbulent structures' scales. In relatively dense cases, large turbulent structures of the spanwise patch size occupy non-patch domains, entrain the particles to the sidewall or fasten the particle exchange at the VP interface. Yet, in relatively sparse cases the length scale of the turbulent structures is about half of that in denser cases, leading to the dispersion of particles near the interface of VP.

What stands out in Fig.21(a)(b) is the high difference between the PDFs of the dense and sparse cases in the vegetated region of the spanwise area of $0 \le Z/Bv \le 1$. There is a peak in the sparse cases, whereas the PDFs decline in the dense patch regions along Z direction. This can be explained by the sparse cases sharing a higher penetration distance for the particles, and hence more particles transport from upstream of the vegetated region but having weaker spanwise dispersion due to the relative weak turbulent structures. For the dense cases, stronger and larger vortices entrain deeper into the VP and carry the particles away, leading to the gradual decline of the PDF span-wisely.

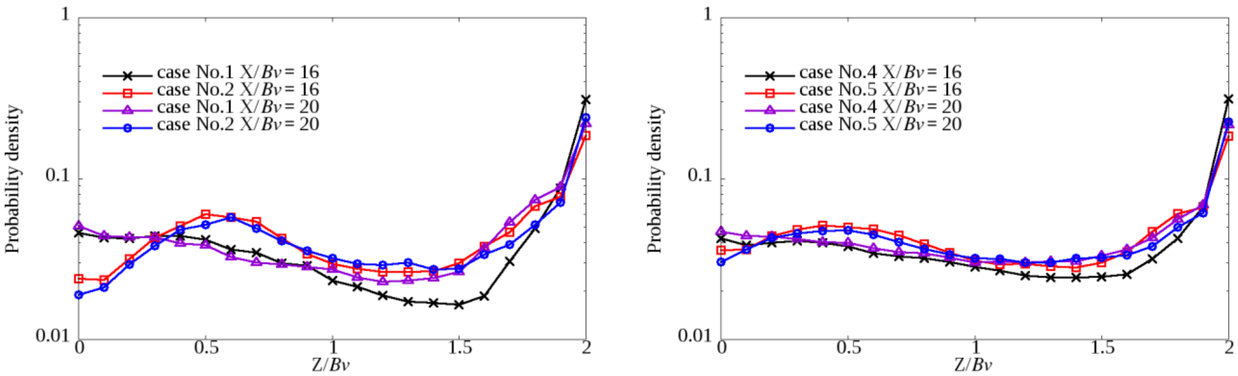

(a) (b)

Fig.22 (a) Probability density functions in spanwise (Z) located in region R8 ($4 \le X \le 5$) in case No.1 and case No.2; (b) Probability density functions in spanwise (Z) located in region R8 ($4 \le X \le 5$) case No.4 and case No.5.

(iv) The wakes of VP region, $16 \le X/Bv \le 24$

The key feature in this region is that the large wakes of the VP size occupy this region, leading to even stronger mixing effects than those upstream of the mixing layer. In the VP wake of region R8, the PDFs tend to return to a uniform distribution because of transport from the spanwise neighbour region. As expected, those particles transport are quicker in dense cases than in sparse cases.

4.2.2 The variance of particle distribution

Turbulent structures within and without a vegetation region are highly anisotropic (Penna et al., 2020, Caroppi et al., 2018, Cui et al., 2008). The distribution of the particles is non-uniform along the vortices' development, as also found by previous studies. For example, De Marchis et al., (2016) found that particles distribute non-uniformly along with vortices' development in a channel bed with roughness. Hu et al., (2002) discussed the particles' uneven dispersion in a spatial developing mixing layer. In current study, the particle dispersion a partially vegetated channel flow is investigated. To quantify this uneven distribution in the spatial and temporal spaces, the variance of PDF is defined. The variance of spanwise (Z) PDF is investigated along the streamwise location to characterize the statistics in different regions. The definition is presented in Eq.(18).

$$Var(\frac{z_i}{Bv}) = \frac{\sum_{i=1}^{N}(f(z_i) - \overline{f(z_i)})^2}{N \cdot \overline{f(z_i)}^2}, \tag{18}$$

where $f(z_i)$ is the PDF at z_i spanwise location, $\overline{f(z_i)}$ is the time-averaged $f(z_i)$, N is the PDF sample times of one specific region $[z_i - \frac{Bv}{M}, z_i + \frac{Bv}{M}] \bigcap [x, x+2Bv]$.

The physical interpretation of the variance of PDF is the normalised fluctuation intensity of PDF profiles in one certain region, which is highly relevant to the uneven distribution of particles in the upstream location. High value of the variance of PDF indicates that particles are moving as parcels, carried by the periphery of large size eddies, and behave with a preferential concentration in a spatial region (De Marchis et al., 2016, Gualtieri et al., 2009, Hu et al., 2002).

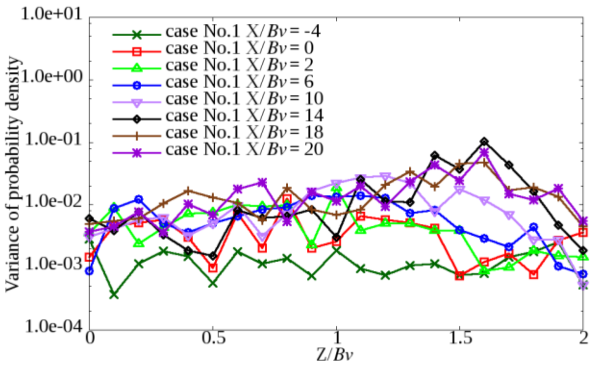

(a) Case No.1

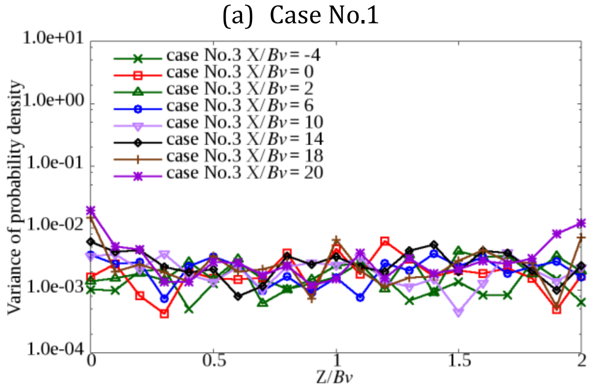

(b) Case No.3

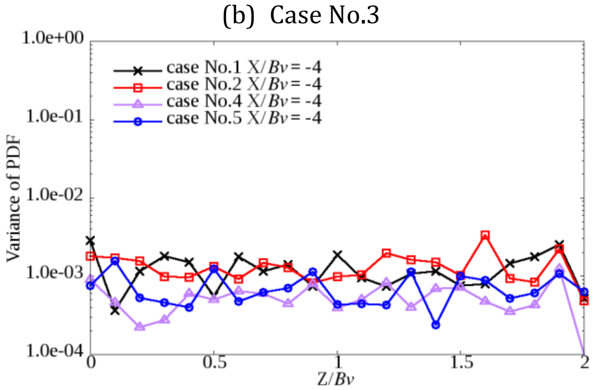

(c)

Fig.23 (a) the variance of PDF in spanwise(Z) located in the whole streamwise region(-4≤X/*Bv*≤20) in case No.1; (b) the variance of PDF in spanwise(Z) located in the whole streamwise region(-4≤X/*Bv*≤20) in Case No.3; (c) the variance of PDF in spanwise (Z) located in region R1 (X/*Bv*=-4) Case No.1, Case No.2, Case No.4 and Case No.5.

What can be clearly seen in Fig.23(a) is the significant growth of the variance of PDF as the observation region moves from R1 to R8 stream-wisely (-4≤X/*Bv*≤20). This trend indicates that the presence of vegetation continuously interrupts the flow condition in the streamwise direction, leading to more intensive turbulent flow events and higher non-uniform particle parcels' distribution. However, this variance of PDF decays after the end of the VP region in the streamwise direction, as seen by comparing the values between the X/*Bv*=14 and X/*Bv*=18. By contrast, Fig.23(b) illustrates that the variance of PDFs stays at a relatively low level in the bare channel of Case No.3 in both the spanwise and streamwise directions, as compared with the vegetated Case No.1.

(i) The diverging flow region

In this region, the spanwise flow can be categorized into three patterns: wakes region having length scale of the stem's diameter in the VP (R3, 0≤Z/*Bv*≤1), the onset of mixing layer region with growing but small vortices (R2, 1≤Z/*Bv*≤1.4~1.6), as well as the uninterrupted region out of the mixing layer (R2, 1.4~1.6≤Z/*Bv*≤2), as displayed in Fig.24(a)(b). There is an over 50% increase of the variance of PDF in the VP region (R3) and mixing layer region (R4) except for the mixing layer outer region (R4), as compared with the upstream variance profiles in R1 region (Fig.24(b)). The plots of variance also show that the width of the mixing layer region increases from 1≤Z/*Bv*≤1.5 to 1≤Z/*Bv*≤1.6 in X/*Bv*=0 and X/*Bv*=2 respectively.

Furthermore, the dense Cases No.1, No.4 always experience a higher variance than that of the sparse cases No.2 case No.5, accordingly, owing to relatively larger scale vortices shedding from the larger stems' diameter in denser cases. Larger turbulent structures have stronger dispersion capability.

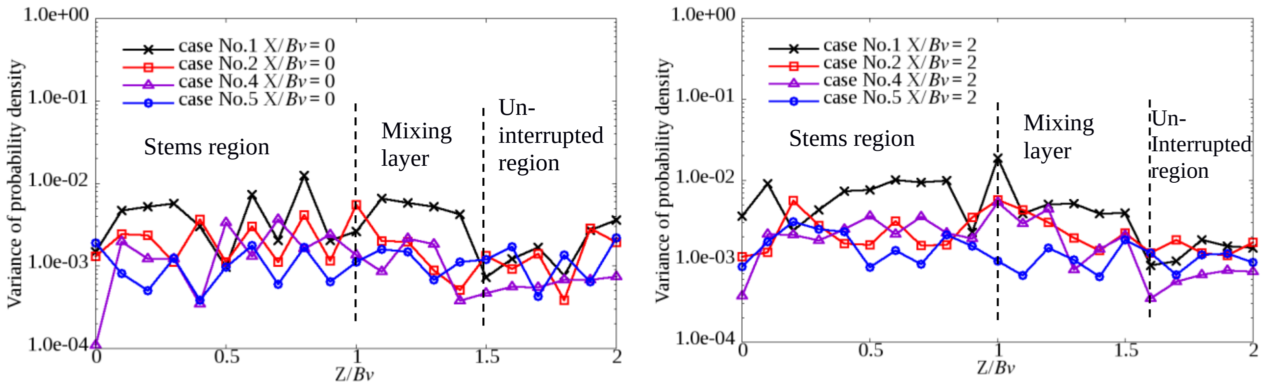

(a) (b)

Fig.24 (a) the variance of PDF in spanwise (Z) located in region R2, R3 (X=0) of cases No.1, No.2, No.4 and No.5; (b) the variance of PDF in spanwise (Z) located in region R2, R3 (X/*Bv*=2) cases of No.1, No.2, No.4 and No.5.

(ii) The mixing layer developing flow region

Making the comparison in the streamwise direction, the variance of the downstream profile

(X/Bv=10) is slightly larger than that of the upstream (X/Bv=6) due to the developing characteristics of the flow pattern. For the span-wise variance distribution in the developing region, there are noticeable higher variance values than that in the VP region, mainly resulting from the mixing effects. Larger scale eddies highly redistribute particles as parcels along the periphery of large eddies. Moreover, the *Dn* behaves as an active factor to increase the variance in the non-vegetated region. As shown in Fig.25(a)(b), the dense cases have a slightly stronger variance in contrast with the sparse cases, respectively, in the corresponding locations, which indicates that the PDF variance is controlled by the dominant eddy scales.

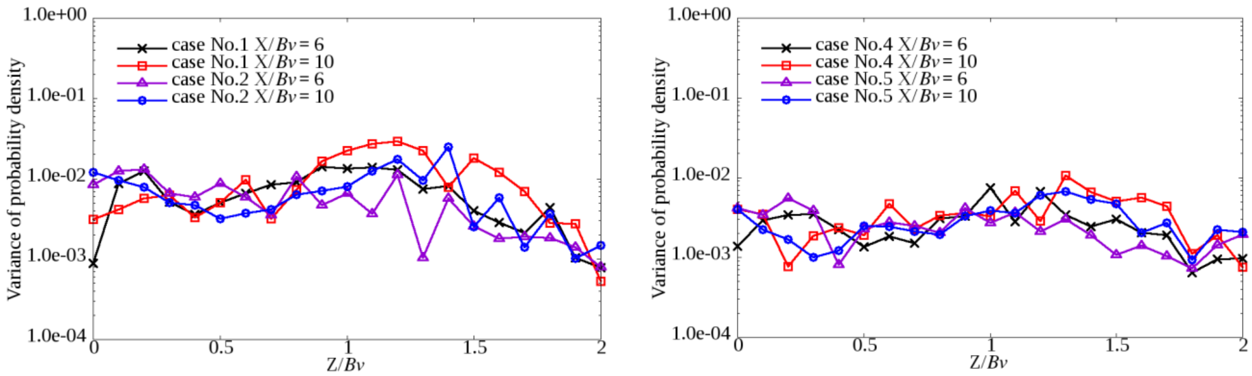

(a) (b)

Fig.25 (a) the variance of PDF in spanwise (Z) located in region R4, R5 (X/Bv=6 and X/Bv=10) case No.1 and case No.2. (b) the variance of PDF in spanwise (Z) located in region R4, R5 (X/Bv=6 and X/Bv=10) case No.4 and case No.5.

(iii) The mixing layer fully developed region

Generally, the variance values in the fully developed region are 20% more than their counterparts in the developing region. Detailed differences are discussed hereafter. Displayed in Fig.26, there is a low point of the variance in the middle region of VP (Z/Bv=0.5). This is because the uniformly distributed stems act as 'filters' and their wakes improve the uniformity of particles as they penetrate through the VP. Also, the 'wiggles' of variances that happen in the flow region (R3) of the VP are diminished in the developed region (R7). This is because of the accumulation of superposition effects of the stem-scale wakes. In the non-vegetated region, the peaks of variances move from the nearside of the interface (1.1≤Z/Bv≤1.3) to the middle of this region (1.4≤Z/Bv≤1.5) where a large scale turbulent flow pattern dominates this phenomenon, as displayed in Fig.11(a).

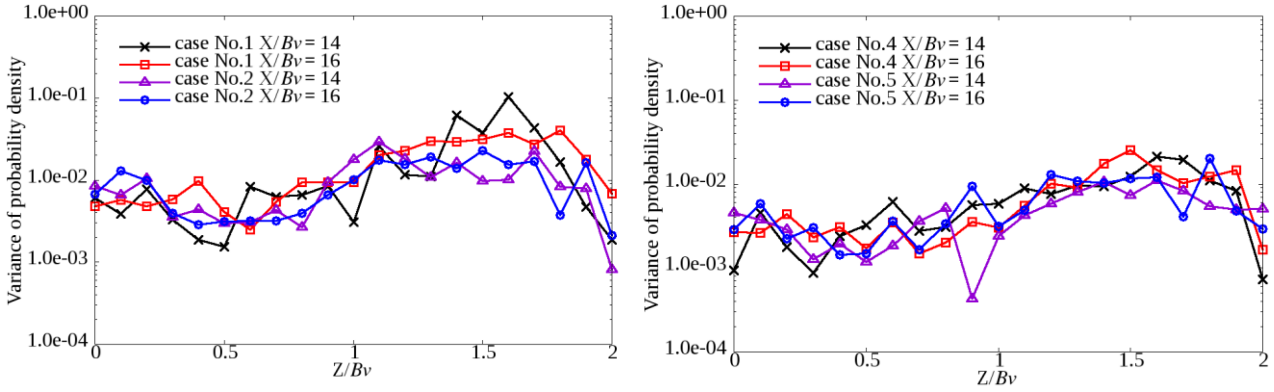

(a) (b)

Fig.26 (a) the variance of PDF in spanwise (Z) located in region R6, R7 (X/*Bv*=14 and X/*Bv*=18) of cases No.1 and No.2. (b) the variance of PDF in spanwise (Z) located in region R6, R7 (X/*Bv*=14 and X/*Bv*=18) cases No.4 and No.5.

(iv) The wake of the VP region

What is interesting in Fig.27 is the collapse of the lines in the non-vegetated region of the various cases and even in different streamwise locations, as compared to the developing and developed regions in Figs.25 and 26. This indicates that the decay of the large vortices is quite slow after the end of VP, the size of turbulent structures nearly unchanged along the wakes of VP (18≤X/*Bv*≤20), as shown in Fig.12. Next, we can also observe that the *Dn* nearly plays no difference between the corresponding case group (No.1~3) and case group (No.4~6). However, the effects of the inlet channel condition (quantified by Re_h) and the Stokes number alter the maxima of the variances between case No.1 to case No.4 and case No.2 to case No.5, where each pair has the same geometry but different Re_h and Stk. Additionally, there is an augmentation of the low points of variance in the patch region (0≤Z/*Bv*≤1) after the VP blockage ended, and relatively large wake eddies can reach this region and transport the particles more uniformly.

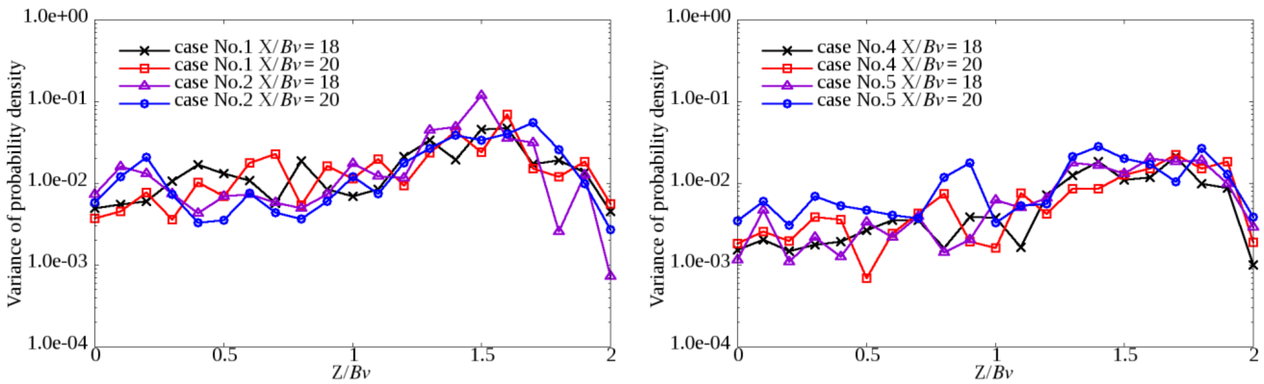

(a) (b)

Fig.27 (a) the variance of PDF in spanwise (Z) located in region R8 (X/*Bv*=18 and X/*Bv*=20) of cases No.1 and No.2. (b) the variance of PDF in spanwise (Z) located in region R8 (X/*Bv*=18 and X/*Bv*=20) of cases No.4 and No.5.

4.3 The vertical entrainment effect and retention effect of VP

4.3.1 The vertical entrainment of particles in VP

In this study, the vertical entrainment effect is defined as an upward motion of suspended particles from the lower water volume to the higher water volume. It is highly interesting that the vegetation patch moves the particles upwardly, while the particles pass through the vegetation patch as illustrated in Fig.28(a)(b). Previous studies observed the resuspension of particles in sparse submerged vegetation (Luhar et al, 2008, Van Katwijk et al., 2010, Lawson et al., 2012). Luhar believed that the resuspension happens in a VP whose *Dn* is less than 0.1 in submerged vegetation condition, because of the mixing layer can penetrate the vegetation layer and touch the riverbed. However, in the present research, the upward entrainment of particles also happens in the sparse emergent vegetation condition (*Dn*=0.063 and 0.025 for Case No.1 and Case No.2 respectively).

(a) Case No.1

(b) Case No.2

(c) Case No.3

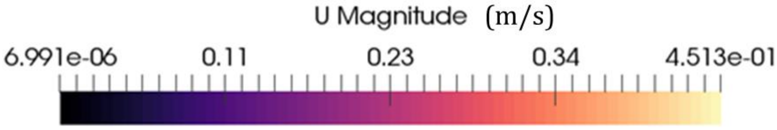

Fig.28 (a) the side view of particle distribution in Case No.1 (a channel with partial vegetation). (b) the side view of particle distribution in Case No.2 (a channel with partial vegetation). (c) the side view of particle distribution in Case No.3 (a channel without vegetation). (a)(b)(c) share the same inlet conditions including the flow condition and particle releasing condition except for the VP. The height of these contour plots is displayed as twice of original ones to increase the clarity.

To quantify the difference in particle concentration of Cases No.1~2, the vertical particles distribution profiles are plotted along the VP region for various streamwise locations in Fig.29.

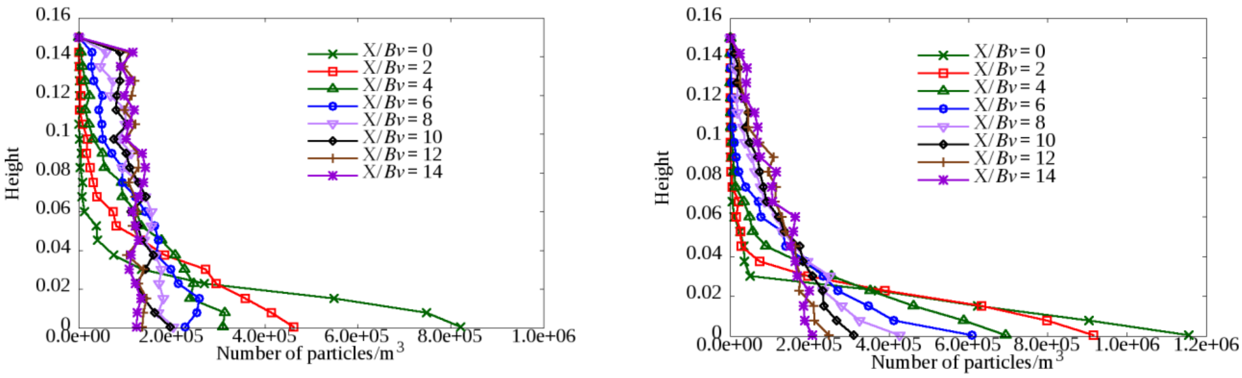

(a) (b)

Fig.29 (a) the vertical particles distribution profiles are plotted along the stream-wisely (0≤X/*Bv*≤14) in the VP region in Case No.1. (b) the vertical particles distribution profiles are plotted along the stream-wisely (0≤X/*Bv*≤14) in the VP region in Case No.2.

In the region (R3 and R4, 0≤X/*Bv*≤12), the concentration profiles quickly vary in the near-bed region, while the particles are gradually transported to higher locations. It is interesting to find that Case No.1 exerts stronger upward suspension capability than that of Case No.2, since the *Dn* of the No.1 is higher than No.2. This observation completes the previous understanding that vegetation does not always have a strong ability to promote sediment deposition.

In the region (R7, 12≤X/*Bv*≤16), the vertical particle distribution profiles reach to a fully developed state. For Case No.1, the vertical distribution is quite uniform, and the profile is significantly reshaped by the vegetation compared to the profile of the upstream non-vegetated region (R1). The reshaping processes of the particle profile is faster than that of Case No.2, as shown in Fig.29(b). This numerical finding indicates that the presence of vegetation unifies the vertical concentration profiles, which is consistent with the experimental result of Lu (2008) that the vertical distribution of suspended sediment in a vegetated channel is obviously more uniform than that in the non-vegetated channel flow. However, the present simulation results indicate the higher *Dn* clearly promotes the uniformity of vertical concentration on the condition that $Dn<0.1$.

Comparing the results of Case No.1 and Case No.2, the sparse VP in Case No.2 also suspends the particles but with less upward entrainment effect. As shown in Fig.28(c), the non-vegetated Case No.3 with same flow condition and suspended sediment inlet condition was also simulated. The vertical concentration profile stays unchanged along the whole domain and no upward entrainment event happens, which indicates the upward suspension role of the sparse vegetation ($Dn<0.1$).

The physical mechanism of this vertical entrainment of particles are explained as follows. As can be seen in Fig.28(a)(b), the upward entrainment of particles gradually happens while the particles pass through the emergent VP. This process is for the first time numerically predicted and presented to the best of the author's knowledge. Li et al., (2020) pointed out that vertical entrainment effect of sediment by flow depended on the vertical velocity component. They also argued that turbulent kinetic energy (TKE) could cause the fine sediment to re-suspend in the process of settling and thus to oscillate in a certain vertical range. Therefore, both the distributions of the vertical velocity and TKE are explored and discussed separately as follows.

Though the spatial averaged streamwise velocity drastically decreased, the vertical entrainment of particles can be explained as the effects of vertical velocity generated by the flow-vegetation-riverbed interactions, i.e., the turbulent horseshoe structures. The vertical velocity contours are displayed and compared in Fig.30. The contour plot of vertical velocity where larger than the settling velocity (0.005m/s) is marked as yellow or light colour, occupies most of the VP.

The velocity difference between a particle and surrounding flow produces a force. A vertical velocity component larger than the particle's still water deposition velocity means that the upward force component is larger than the effective weight (including the effects of buoyancy) of this particle. Thus, an upward acceleration is produced. Then, a time integration of this upward acceleration leads to an upward velocity and displacement. The vertical velocity entrains the particles from the lower particle-rich region to the upper particle-less region. Also, a higher *Dn* leads to a larger area in the slices in Fig.30 where vertical velocity larger than the deposition velocity when comparing Fig.30(a) to Fig.30(b) and Fig.30(c) to Fig.30(d), which implies why higher *Dn* (*Dn*<0.1) entrains fine sediment vertically faster.

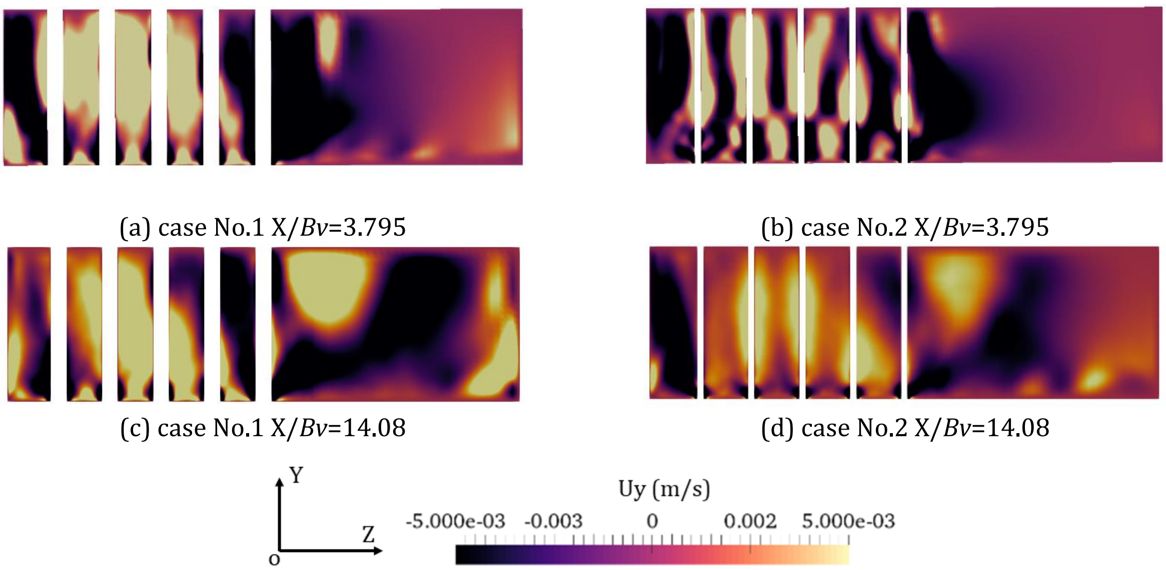

Fig.30 (a) and (b) are the contours of time-averaged vertical velocity Uy (m/s) in the VP region R2, R3 (X/*Bv*=3.795) in Case No.1 and Case No.2 respectively. (c) and (d) are the contours of time-averaged vertical velocity Uy (m/s) in the VP region R6, R7 (X/*Bv*=14.08) in Case No.1 and Case No.2 respectively. The white lines are the vegetation stems. The five white lines are the stems in each figure.

Nino and Garcia (1996) pointed out that the sediment particles were picked up from the bed by flow ejection events that were related to the near-bed lift force. Latest studies show that the turbulent kinetic energy (TKE) can be a good indicator in predicting the upward motion of particles from the bed. Yang et al., (2016) suggested that near-bed TKE may have a higher effect than bed shear stress on the initiation of sediment motion. The TKE model works both for the bare bed and vegetated bed. Tseng and Tinoco, (2021) believed the TKE can indicate the total turbulence generated from vegetation, bed, and coherent structures and hence calculated the effective bed shear velocity. Therefore, the instantaneous contour plots of TKE on slice X/*Bv*=3.795 and 14.08 are presented in Fig.31 as a representative.

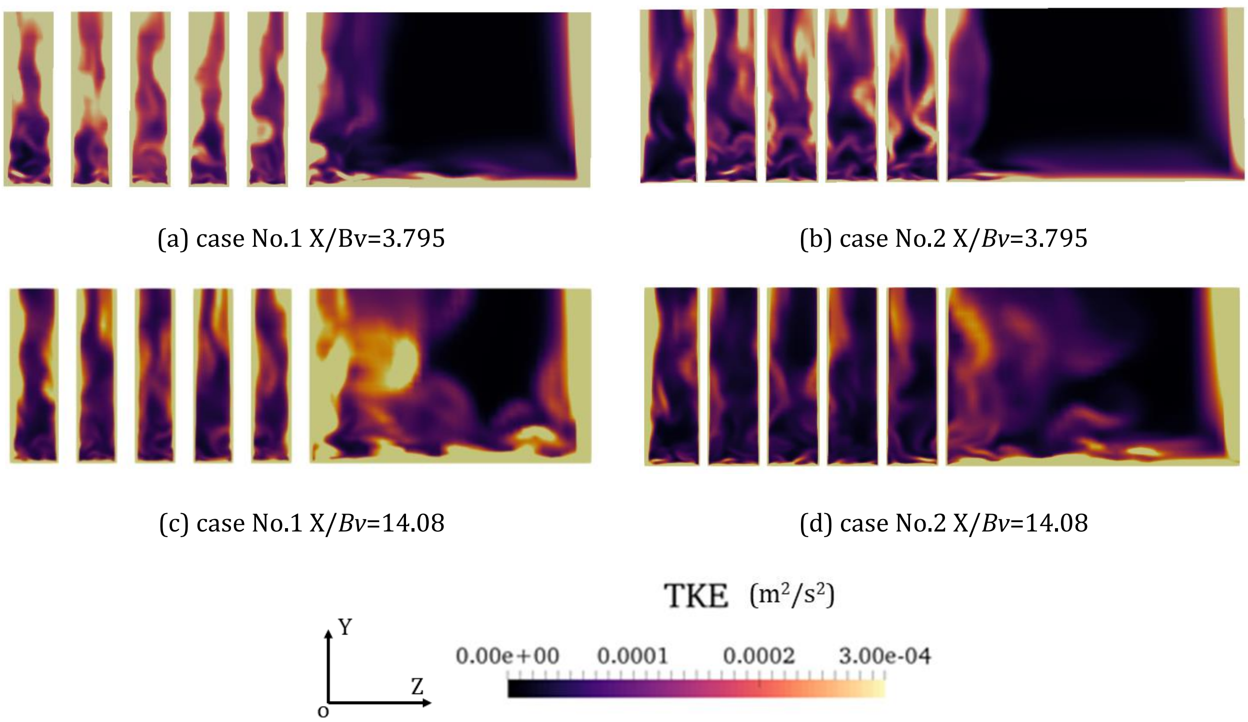

Fig.31 (a) and (b) are the contours of instantaneous turbulent kinetic energy (TKE) (m^2/s^2) in the VP region R2, R3 (X/*Bv*=3.795) in case No.1 and case No.2 respectively. (c) and (d) are the contours of instantaneous turbulent kinetic energy (TKE) (m^2/s^2) in the VP region R6, R7 (X/*Bv*=14.08) in case No.1 and case No.2 respectively. The white lines are the vegetation stems. The five white lines are the stems in each figure.

As shown in Fig.31, the presence of stems increases the TKE in the vegetated region, thus promotes the upward suspension of suspended sediments. Case No.1 with the higher vegetation density has a stronger TKE that may present a stronger capability of resuspending particles than that of Case No.2. It is worth to mention that the high regions of TKE are the boundary layer or wakes regions of stems.

In summary, all previous studies agree that the upward entrainment of particles is produced by the turbulent structures or turbulent properties. Some researchers believe that the TKE is a good indicator or explanation of the upward motion of particles, while some researchers (Li et al., 2020) believe the vertical (upward) velocity component of secondary flow can be more of the cause of the upward motion of particles. Moreover, other indicators including the turbulence skewness factors and turbulent shear stress are also used to explain the vertical motion of particles. The authors of this paper prefer the explanation by vertical velocity, but still believe that further studies are needed to answer this open question.

4.3.2 The retention of particles in vegetation patch

Comparisons were made between vegetated and non-vegetated cases; the presence of vegetation may make the particles' concentration higher in the patch region than in the same region with no vegetation canopy. Besides, the mixing layer region produced by vegetation contains less particles because of the centrifugal effects of vortices inertially moving particles away from the centre region of the vortex region (Hu et al., 2002). Therefore, we conclude that the vegetation patch in a natural channel does not simply increase or decrease the particles concentration.

Moreover, because of the upward suspension of particles, the particle concentration is significantly higher than that in the same region of the non-vegetated channel for high vertical locations i.e., $Y/D_p \geq 500$, as illustrated in Fig.32(a)(b). This retention of particles in the channels maintains the evolution of ecosystem. However, in the low location $Y/D_p \leqslant 30$ the concentration is drastically lower than that in the non-vegetated case, as shown in Fig.32(c)(d). This completes the previous understanding that the particles' concentration is always higher in the vegetated regions than in the non-vegetated regions or cases.

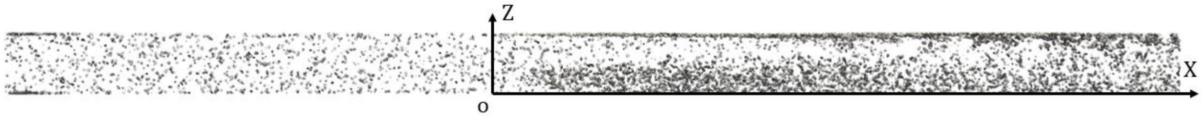

(a) The vegetated case No.1 Y/D_p=500

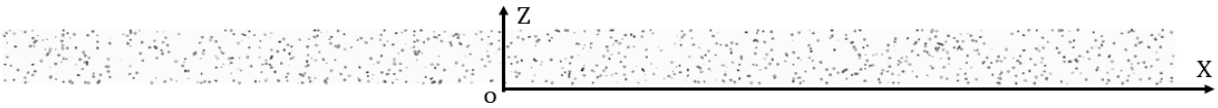

(b) The non-vegetated case No.3 Y/D_p=500

(c) The vegetated case No.1 Y/D_p=30

(d) The non-vegetated case No.3 Y/D_p=30

Fig.32 (a) the horizontal slice of case No.1 in Y/D_p=500. (b) the horizontal slice of case No.3 in Y/D_p=500. (c) the horizontal slice of case No.1 in Y/D_p=30. (d) the horizontal slice of case No.3 in Y/D_p=30. Black points denote the particles in this slice. The size of the points is 100 times bigger than their real size for clarity.

5. Conclusions

The transportation of particles in a partially vegetated straight channel is investigated using high-fidelity CFD(LES)-DPM method. The distribution of particles in the flow-parallel edge of the VP has highly interesting dispersion behaviour. The particles are uniformly distributed in the spanwise direction, upstream of the vegetated region. Turbulent structures grow in the mixing layer on the edge of vegetation patch, resulting in depletion of particles in this layer. Canopy with a higher density generates more turbulent structures, exerting stronger spanwise dispersion effects in the VP outer region (R4) and promotes spatial uneven distribution of particles.

Another new finding is that particles' distribution highly coincides with the contour margin of vertical vorticity component in the edge of mixing layer, especially in the near-bed region. This is because particles prefer to stay in a lower vorticity region and gather at the mixing layer edge. However, as the locations of sample plane (slice) move away from the channel bed, the agreement between the particles' distribution and vertical component of vorticity becomes blurred. This is because of the turbulent structures developing from the channel bed that interrupt particles' distribution.

The Probability Density Function (PDF) was defined to quantify the particles' spanwise distribution. When comparing the PDF of the same location between the relative dense cases to sparse cases, respectively, all denser cases showed lower PDF values in the mixing layer of the developing region (R4) and developed region (R6).

The variance of PDF was defined to quantify the normalised fluctuation intensity in a target zone, which is highly relevant to the nature of particles' uneven distribution carried by the upstream turbulent structures. A significant growth was observed in the variance of PDF as the observation region moved along the streamwise direction from R1 to R8 regions ($-4 \leq X/Bv \leq 20$). This trend indicates that the presence of vegetation continuously interrupts the flow condition in the streamwise direction, leading to more intensive turbulent flow events and higher non-uniform particle parcels' distributions both temporally and spatially.

The variance of PDF distribution in the developing region (R4) is markedly higher than that in the VP's region R5, mainly due to the mixing effects. The vegetation density behaves as an active factor to increase the variance in non-vegetated region. Moreover, in the non-vegetated region, the peaks of variances move from the nearside of the interface ($1.1 \leq Z/Bv \leq 1.3$) to the middle of this region ($1.4 \leq Z/Bv \leq 1.5$) where large scale turbulent flow patterns dominate this phenomenon.

The particle upward suspension by vegetation patch is simulated during the flow pass through the stems. The relative dense cases (Dn=0.063) have a stronger upward suspension effect than relative sparse cases (Dn=0.025), under the condition that Dn<0.1. It agrees with previous argument of Dn=0.1 as a threshold assuming drag coefficients of stems as 1.0 (Nepf. 2012).

Because of the upward suspension of particles in vegetated cases, the particle concentration is pronounced higher than the same region in non-vegetated channel for same vertical locations i.e., $Y/D_p \geq 500$. However, in the low location $Y/D_p \leqslant 30$ the concentration is drastically lower than in the non-vegetated cases.

In future research, the influence of the flexibility of vegetation (Wang et al., 2019) and the bending effects of open channel (Wang et al., 2020) on suspended sediments transportation will be considered.

6. Nomenclature

a	The frontal area per canopy volume (m^2)
Bv	The spanwise length scale of the vegetation patch (m)
C_d	The drag coefficient for a single stem
C_l	The lift coefficient for a single stem
d	The diameter of a single stem (mm)
Dn	Vegetation density
D_p	The diameter of particles (m)
$f()$	The probability density function (PDF)
$f(z_i)$	The PDF at z_i spanwise location
$\overline{f(z_i)}$	The time-averaged $f(z_i)$
Fr	The channel Froude number
F_i^f	Particle-fluid interaction forces (N)
F_i^g	Gravity of particle (N)
F_{ij}^c	Contact force acting from object j (particle or wall) to particle i (N)
F_{ik}^{nc}	Non-contact force acting on the particle i by particle k or other sources (N)
F_d	Drag (N)

$F_{\nabla p}$	Pressure gradient (pa/m)
$F_{\nabla \cdot \tau}$	Viscous forces (N)
F_{vm}	Virtual mass forces (N)
F_B	Basset force (N)
F_{saff}	Saffman force (N)
F_{Mag}	Magnus force (N)
g	Gravity (N)
h	The depth of channel (m)/height of plant
LES	Large Eddy Simulation
L	The length of the whole domain in streamwise direction (m)
L_c	The canopy drag length scale
M_{ij}	Torque acting from object *j* (particle or wall) to particle *i* (Nm)
N	The PD sample times of one specific region
$\overline{N}_i$	The time-averaged number of particles in the ith subregion
PDF	Probability Density Function
PDF_{max}	The maximum value of the PDF
PDF_{min}	The minimum value of the PDF
R1	The upstream flow of VP
R2	The diverging flow region
R3	The front part of the VP
R4	The developing region of turbulent mixing layer
R5	The turbulent structures fully developed in VP
R6	The fully developed region for the mixing layer
R7	The turbulence structures gradually attenuate
R8	The wake region of VP
Re_d	The Reynolds number based on the diameter of stem
Re_h	The channel Reynolds number
Re_p	The particle Reynolds number
RST	Relative Stable Test
S	The concentration of particles (number/m^3)
S_p	Volumetric fluid-particle interaction force (N/m^3)
S_a	The concentration of the Y/h=0.5
Stk	Stokes number of released particles
t	Time (s)
U_f	Fluid phase velocity (m/s)
U_p	Velocity of particles (m/s)
U_i^p	Translational velocity of i_{th} particle (m/s)
U_{mean}	Averaged inlet velocity (m/s)
Uy	The vertical component of flow velocity (m/s)
Var	The variance of the PDF
V_{stems}	The volume of stems (m^3)
V_{patch}	The volume of the bulk of the patch region (m^3)

X	The streamwise direction/coordinate
X_D	The length scale of the diverging flow in streamwise direction
Y	The vertical direction/coordinate
$Y+$	Dimensionless wall distance
z_i	The spanwise coordinate, in the i_{th} subregion
Z	The spanwise direction/coordinate
α	Scale factor α = 2.3 ± 0.2
α_f	Fluid phase fraction
β	Scale factor β= 1.5 ± 0.2
τ_f	Fluid-phase viscous stress tensor (pa)
ω_i	Angular velocity (rad/s)
Δr	The size of first layer mesh around the single stem (mm)
υ	Viscosity of water (m^2/s)
ρ_f	The density of fluid (kg/m^3)
ρ_p	The density of particles (kg/m^3)

7. References

Agawin, N. S., Duarte, C. M., 2002. Evidence of direct particle trapping by a tropical seagrass meadow. Estuaries, 25(6), 1205-1209.

Banko, A. J., and Eaton, J. K.,2019. A frame-invariant definition of the Q-criterion.

Bertoldi, W., Welber, M., Gurnell, A. M., Mao, L., Comiti, F., Tal, M., 2015. Physical modelling of the combined effect of vegetation and wood on river morphology. Geomorphology, 246, 178-187.

Belcher, S.E., N. Jerram, and J.C.R. Hunt. 2003. Adjustment ofa turbu- lent boundary layer to a canopy of roughness elements. Journal of Fluid Mechanics 488: 369–398

Braza, M., Chassaing, P., Minh, H.H., 1986. Numerical study and physical analysis of the pressure and velocity fields in the near wake of a circular cylinder. Journal of fluid mechanics 165, 79–130.

Cameron, S., Nikora, V., Albayrak, I., Miler, O., Stewart, M., & Siniscalchi, F., 2013. Interactions between aquatic plants and turbulent flow: A field study using stereoscopic PIV. Journal of Fluid Mechanics*, 732*, 345-372. doi:10.1017/jfm.2013.406

Caroppi, G., Gualtieri, P., Fontana, N., Giugni, M., 2018. Vegetated channel flows: Turbulence anisotropy at flow–rigid canopy interface. Geosciences, *8*(7), 259.

Caporaloni, M., Tampieri, F., Trombetti, F., Vittori, O., 1975. Transfer of particles in nonisotropic air turbulence. Journal of the atmospheric sciences 32, 565–568.

Chen, S.-C., Kuo, Y.-M., Li, Y.-H., 2011. Flow characteristics within different configurations of submerged flexible vegetation. Journal of Hydrology 398, 124–134.

Chen, Z., C. Jiang, and H. Nepf. 2013. Flow adjustment at the leading edge of a submerged aquatic canopy. Water Resources Research 49: 5537–5551. doi:10.1002/wrcr.20403.

Cheng, C., Song, Z., Wang, Y., Zhang, J., 2013. Parameterized expressions for an improved Rouse equation. International Journal of Sediment Research 28, 523–534.

China, the Yellow River Basin Ecological Protection and High-quality Development, 2019. http://www.china.org.cn/china/2020-09/01/content_76656613.htm

Clarke, S.J., Wharton, G., 2001. Sediment nutrient characteristics and aquatic macrophytes in lowland English rivers. Science of the Total Environment 266, 103–112.

Corenblit, D., Tabacchi, E., Steiger, J., Gurnell, A.M., 2007. Reciprocal interactions and adjustments between fluvial landforms and vegetation dynamics in river corridors: a review of complementary approaches. Earth-Science Reviews 84, 56–86.

Crowe, C.T., Schwarzkopf, J.D., Sommerfeld, M., Tsuji, Y., 2011. Multiphase flows with droplets and particles. CRC press.

Cui, J., Neary, V. S., 2008. LES study of turbulent flows with submerged vegetation. Journal of Hydraulic Research, 46(3), 307-316.

Curran, J.C., Hession, W.C., 2013. Vegetative impacts on hydraulics and sediment processes across the fluvial system. Journal of Hydrology 505, 364–376.

De Marchis, M., Milici, B., Sardina, G., Napoli, E., 2016. Interaction between turbulent structures and particles in roughened channel. International Journal of Multiphase Flow 78, 117–131.

Diplas, P., Dancey, C.L., Celik, A.O., Valyrakis, M., Greer, K., Akar, T., 2008. The role of impulse on the initiation of particle movement under turbulent flow conditions. Science 322, 717–720.

Durán, O., Andreotti, B., Claudin, P., 2012. Numerical simulation of turbulent sediment transport, from bed load to saltation. Physics of Fluids 24, 103306.

Elghannay, H., Tafti, D., 2018. LES-DEM simulations of sediment transport. International Journal of Sediment Research 33, 137–148.

Escauriaza, C., Sotiropoulos, F., 2011. Lagrangian model of bed-load transport in turbulent junction flows. Journal of Fluid Mechanics 666, 36.

Fernandes, C., Semyonov, D., Ferrás, L.L., Nóbrega, J.M., 2018. Validation of the CFD-DPM solver DPMFoam in OpenFOAM through analytical, numerical and experimental comparisons. Granular Matter 20, 64.

Follett, E.M., Nepf, H.M., 2012. Sediment patterns near a model patch of reedy emergent vegetation. Geomorphology 179, 141–151.

Gacia, E., Duarte, C. M., 2001. Sediment retention by a Mediterranean Posidonia oceanica meadow: the balance between deposition and resuspension. Estuarine, coastal and shelf science, 52(4), 505-514.

Garcia‐Mora, M. R., Gallego‐Fernández, J. B., García‐Novo, F., 1999. Plant functional types in coastal foredunes in relation to environmental stress and disturbance. Journal of Vegetation Science, 10(1), 27-34.

Graf, W.H., Cellino, M., 2002. Suspension flows in open channels; experimental study. Journal of hydraulic research 40, 435–447.

Gualtieri, P., Picano, F., Casciola, C.M., 2009. Anisotropic clustering of inertial particles in homogeneous shear flow. J. Fluid Mech. 629, 25–39.

Gu, J., Shan, Y., Liu, C., Liu, X., 2019. Feedbacks of flow and bed morphology from a submerged dense vegetation patch without upstream sediment supply. Environmental Fluid Mechanics, 19(2), 475-493.

Hu, Z., Luo, X., & Luo, K. H., 2002. Numerical simulation of particle dispersion in a spatially developing mixing layer. Theoretical and Computational Fluid Dynamics, 15(6), 403-420.

Huai, W., Xue, W., Qian, Z., 2015. Large-eddy simulation of turbulent rectangular open-channel flow with an emergent rigid vegetation patch. Advances in Water Resources 80, 30–42.

Huai, W., Yang, L., Guo, Y., 2020. Analytical solution of suspended sediment concentration profile: Relevance of dispersive flow term in vegetated channels. Water Resources Research 56, e2019WR027012.

Huai, W., Yang, L., Wang, W.-J., Guo, Y., Wang, T., Cheng, Y., 2019. Predicting the vertical low suspended sediment concentration in vegetated flow using a random displacement model. Journal of Hydrology 578, 124101.

Ji, C., Munjiza, A., Avital, E., Xu, D., Williams, J., 2014. Saltation of particles in turbulent channel flow. Physical Review E 89, 052202.

Kemp, J.L., Harper, D.M., Crosa, G.A., 2000. The habitat-scale ecohydraulics of rivers. Ecological engineering 16, 17–29.

Kim, H.S., Kimura, I., Shimizu, Y., 2015. Bed morphological changes around a finite patch of vegetation. Earth Surface Processes and Landforms 40, 375–388.

Krajnović, S., Davidson, L., 2002. A mixed one-equation subgrid model for large-eddy simulation. International journal of heat and fluid flow 23, 413–425.

Kuerten, J.G., 2016. Point-Particle DNS and LES of Particle-Laden Turbulent flow-a state-of-the-art review. Flow, turbulence and combustion 97, 689–713.

Larsen, L.G., Harvey, J.W., Noe, G.B., Crimaldi, J.P., 2009. Predicting organic floc transport dynamics in shallow aquatic ecosystems: Insights from the field, the laboratory, and numerical modeling. Water Resources Research 45.

Lawson, S.E., McGlathery, K.J., Wiberg, P.L., 2012. Enhancement of sediment suspension and nutrient flux by benthic macrophytes at low biomass. Marine Ecology Progress Series 448, 259–270.

Leonard, L. A., & Croft, A. L. (2006). The effect of standing biomass on flow velocity and turbulence in Spartina alterniflora canopies. Estuarine, Coastal and Shelf Science, 69(3-4), 325-336.

Li, D., Yang, Z., Sun, Z., Huai, W., Liu, J., 2018. Theoretical model of suspended sediment concentration in a flow with submerged vegetation. Water 10, 1656.

Li, D., Yang, Z., Zhu, Z., Guo, M., Gao, W., Sun, Z., 2020. Estimating the distribution of suspended sediment concentration in submerged vegetation flow based on gravitational theory. Journal of Hydrology 124921.

Li, Y., Xie, L., Su, T. C., 2020. Profile of suspended sediment concentration in submerged vegetated shallow water flow. Water Resources Research, 56(4), e2019WR025551.

Liu, C., Nepf, H., 2016. Sediment deposition within and around a finite patch of model vegetation over a range of channel velocity. Water Resources Research, 52(1), 600-612.

López, F., García, M., 1998. Open-channel flow through simulated vegetation: Suspended sediment transport modeling. Water resources research 34, 2341–2352.

Lopez, F., Garcia, M., 1997. Open-channel flow through simulated vegetation: Turbulence modeling and sediment transport. US Army Engineer Waterways Experiment Station.

Lu, S., 2008. Experimental study on distribution law of suspended sediment in water flow of rigid plants (in Chinese). Hohai University. https://doi.org/10.7666/d.y1268411

Luhar, M., Rominger, J., Nepf, H., 2008. Interaction between flow, transport and vegetation spatial structure. Environmental Fluid Mechanics 8, 423.

Marchis, M. D., Milici, B., Sardina, G., Napoli, E., (2016). Interaction between turbulent structures and particles in roughened channel. International Journal of Multiphase Flow*, 78*, 117-131.

Mars, R., Mathew, K., Ho, G., 1999. The role of the submergent macrophyte Triglochin huegelii in domestic greywater treatment. Ecological Engineering 12, 57–66.

Nepf, H.M., 2012. Hydrodynamics of vegetated channels. Journal of Hydraulic Research 50, 262–279.

Nepf, H.M., 2012. Flow and Transport in Regions with Aquatic Vegetation. Annual review of Fluid Mechanics. 44,1, 123-142

Oh, J., Tsai, C.W., 2018. A stochastic multivariate framework for modeling movement of discrete sediment particles in open channel flows. Stochastic environmental research and risk assessment 32, 385–399.

Ortiz, A.C., Ashton, A., Nepf, H., 2013. Mean and turbulent velocity fields near rigid and flexible plants and the implications for deposition. Journal of Geophysical Research: Earth Surface 118, 2585–2599.

Penna, N., Coscarella, F., D'Ippolito, A., Gaudio, R., 2020. Anisotropy in the free stream region of turbulent flows through emergent rigid vegetation on rough beds. Water, 12(9), 2464.

Picano, F., Sardina, G., Casciola, C.M., 2009. Spatial development of particle-laden turbulent pipe flow. Physics of Fluids 21, 093305.

Pilou, M., Antonopoulos, V., Makris, E., Neofytou, P., Tsangaris, S., and Housiadas, C., 2013. A fully eulerian approach to particle inertial deposition in a physiologically realistic bifurcation. Applied Mathematical Modelling, 37(8), 5591-5605.

Pollen, N., Simon, A., 2005. Estimating the mechanical effects of riparian vegetation on stream bank stability using a fiber bundle model. Water Resources Research 41.

Rominger, J.T., Lightbody, A.F., Nepf, H.M., 2010. Effects of added vegetation on sand bar stability and stream hydrodynamics. Journal of Hydraulic Engineering 136, 994–1002.

Rouse, H., 1937. Modern concepts of the mechanics of turbulence. ASCE. Transactions 102.

Sardina, G., Schlatter, P., Brandt, L., Picano, F., Casciola, C.M., 2012. Wall accumulation and spatial localization in particle-laden wall flows. Journal of Fluid Mechanics 699, 50–78.

Schmeeckle, M.W., 2015. The role of velocity, pressure, and bed stress fluctuations in bed load transport over bed forms: numerical simulation downstream of a backward-facing step. Earth Surface Dynamics 3, 105.

Stephan, U., Gutknecht, D., 2002. Hydraulic resistance of submerged flexible vegetation. Journal of Hydrology 269, 27–43.

Sun, R., Xiao, H., 2016. SediFoam: A general-purpose, open-source CFD–DEM solver for particle-laden flow with emphasis on sediment transport. Computers & Geosciences 89, 207–219.

Terrados, J., Duarte, C. M., 2000. Experimental evidence of reduced particle resuspension within a seagrass (Posidonia oceanica L.) meadow. Journal of experimental marine biology and ecology, 243(1), 45-53.

Tseng, C. Y., Tinoco, R. O., 2021. A Two-Layer Turbulence-based Model to Predict Suspended Sediment Concentration in Flows with Aquatic Vegetation. Geophysical Research Letters, e2020GL091255.

Van Katwijk, M.M., Bos, A.R., Hermus, D.C.R., Suykerbuyk, W., 2010. Sediment modification by seagrass beds: Muddification and sandification induced by plant cover and environmental conditions. Estuarine, Coastal and Shelf Science 89, 175–181.

Vreman, A.W., 2015. Turbulence attenuation in particle-laden flow in smooth and rough channels. Journal of Fluid Mechanics 773, 103–136.

Yu, G., Avital, E. J., & Williams, J. J. R., 2008. Large eddy simulation of flow past free surface piercing circular cylinders. *Journal of Fluids Engineering*, *130*(10).

Wang, M., Avital, E. J., Bai, X., Ji, C., Williams J., Munjiza, A., 2019. Fluid–structure interaction of flexible submerged vegetation stems and kinetic turbine blades. Computational Particle Mechanic*s*, **7,** 839–848 (2020). https://doi.org/10.1007/s40571-019-00304-6

Wang, M., Avital, E., Korakianitis T., Williams J., Ai K., 2020. A numerical study on the influence of curvature ratio and vegetation density on a partially vegetated U-bend channel flow. Advances in Water Resources,103843, ISSN 0309-1708.

Wang, X.Y., Xie, W.M., Zhang, D., He, Q., 2016. Wave and vegetation effects on flow and suspended sediment characteristics: A flume study. Estuarine, Coastal and Shelf Science 182, 1–11.

Ward, L. G., Kemp, W. M., Boynton, W. R., 1984. The influence of waves and seagrass communities on suspended particulates in an estuarine embayment. Marine Geology, 59(1-4), 85-103.

White, B.L., Nepf, H.M., 2008. A vortex-based model of velocity and shear stress in a partially vegetated shallow channel. Water Resources Research 44.

White, B.L., Nepf, H.M., 2007. Shear instability and coherent structures in shallow flow adjacent to a porous layer. Journal of Fluid Mechanics 593, 1–32.

Zdravkovich, M.M., 1997. Flow around circular cylinders; vol. i fundamentals. Journal of Fluid Mechanics, 350(1),

pp.377-378.
Zhang, Y., Lai, X., Zhang, L., Song, K., Yao, X., Gu, L., Pang, C., 2020. The influence of aquatic vegetation on flow structure and sediment deposition: A field study in Dongting Lake, China. Journal of Hydrology 584, 124644.
Zhao, F., George, W.K., Van Wachem, B.G.M., 2015. Four-way coupled simulations of small particles in turbulent channel flow: The effects of particle shape and Stokes number. Physics of Fluids 27, 083301.
Zhong, D., Zhang, L., Wu, B., Wang, Y., 2015. Velocity profile of turbulent sediment-laden flows in open-channels. International Journal of Sediment Research, 30(4), 285-296.
Zong, L., Nepf, H., 2012. Vortex development behind a finite porous obstruction in a channel. Journal of Fluid Mechanics 691, 368–391.
Zong, L., Nepf, H., 2011. Spatial distribution of deposition within a patch of vegetation. Water Resources Research 47.

8. Acknowledgement

The first author thanks CSC and QMUL for supporting his Ph.D. studentship. Further acknowledgement is given to the UK EPSRC Turbulence Consortium, grant EP/R029326/1 and the Royal society IEC/NSFC/1181425.